Energy Advances

ROYAL SOCIETY OF CHEMISTRY

PAPER

View Article Online
View Journal | View Issue

Cite this: *Energy Adv.*, 2024, 3, 2377

Numerical modeling and extensive analysis of an extremely efficient $RbGeI_3$-based perovskite solar cell by incorporating a variety of ETL and HTL materials to enhance PV performance

Md. Mojahidur Rahman,[a] Md. Hasan Ali, *[b] Md. Dulal Haque[c] and Abu Zafor Md. Touhidul Islam*[a]

The immense demand for electrical energy motivated us to manipulate solar energy by means of conversion through solar cells (SCs). Advancements in photovoltaic (PV) technology are occurring very rapidly. In recent years, extensive research has been conducted on halide perovskite-based SCs because of their superior optoelectronic properties, enhanced efficiency, lightweight nature, and low cost. However, concerns have arisen regarding their longevity, stability, and commerciality due to the presence of toxic lead (Pb). The most prominent purpose of this investigation is to discover additional efficient, sustainable, and eco-friendly device architectures. In this study, we investigated an all-inorganic, lead-free rubidium germanium iodide ($RbGeI_3$)-based PSC device with the assistance of the SCAPS-1D simulator. Several electron transport layers (ETLs) and hole transport layers (HTLs) were incorporated with the perovskite layer, and an efficient primary structure was discovered. Then, the impact of temperature; back metal work function; series and shunt resistance; surface recombination velocity of carriers; thickness of the perovskite absorber layer, electron transport material (ETM), and hole transport material (HTM); carrier concentration of the perovskite absorber layer, ETM, and HTM; defect density of the perovskite absorber layer, ETM, and HTM; and defect density of the HTL/absorber and absorber/ETL interfaces on the PV performance of the proposed PSC device was analyzed. The optimized device exhibited a power conversion efficiency (PCE) of 30.35%, with superior values for open circuit voltage (V_{oc}), short circuit current density (J_{sc}), and fill factor (FF) of 1.067 V, 33.15 mA cm^{-2}, and 85.82%, respectively. The investigations in this study may be valuable and impactful to solar cell material researchers and move the research interest forward by one step so that experimental work with non-toxic $RbGeI_3$-based PSC devices will be performed in the future.

Received 22nd May 2024,
Accepted 26th July 2024

DOI: 10.1039/d4ya00323c

rsc.li/energy-advances

1. Introduction

Due to extensive population growth, the technological improvement of civilization, and the progression of developing countries worldwide, the increasing demands for electronic devices as well as electricity are extensively increasing the consumption and utilization of global energy.[1–3] It has been predicted that in 2050, the demand for the consumption of energy will reach a level of about 30 terawatts (TW).[1,4,5] This substantial need for energy is primarily met by the use of fossil fuels, which continue to account for more than 80% of the global energy system.[6–8] Due to the burning of fossil fuels, a tremendous amount of CO_2 has been exhausted and has contaminated the ecosystem, causing climate change, global warming, and the greenhouse effect.[9–13]

The current challenge in photovoltaics is to fabricate eco-friendly solar cells with a higher value of efficiency for the conversion of photon energy, as well as longevity, stability, commerciality, and cost-effectiveness.[14] There are several types of solar cells (SCs) that have technologically evolved, including silicon (Si),[15] cadmium telluride (CdTe),[16] antimony selenide (Sb_2Se_3),[17] molybdenum sulfide (MoS_2),[1] copper indium gallium selenide (CIGS),[18,19] copper zinc tin sulfide (CZTS),[20] copper iron tin sulfide (CFTS),[21,22] copper indium telluride ($CuInTe_2$),[23] polymer, inorganic metal chalcogenide, quantum dot (QD), dye-sensitized solar cells (DSSCs), and perovskite-based solar cells.[24–26]

[a] *Department of Electrical and Electronic Engineering, University of Rajshahi, Rajshahi-6205, Bangladesh. E-mail: hasan@brur.ac.bd, touhid.eee@ru.ac.bd*
[b] *Advanced Energy Materials and Solar Cell Research Laboratory, Department of Electrical and Electronic Engineering, Begum Rokeya University, Rangpur, Rangpur-5400, Bangladesh*
[c] *Department of Electronics and Communication Engineering, Hajee Mohammad Danesh Science and Technology University, Dinajpur-5200, Bangladesh*

Among the different types of PV materials, organic–inorganic (hybrid) halides exhibit various remarkable properties such as a high absorption coefficient, simple synthesis, adjustable band gap, a larger value of diffusion length, efficient solution processing ability, and low cost, and they are desirable materials because of these remarkable properties.[24,25] The first innovation of organic–inorganic halide perovskite-based solar cells (PSCs) was in 2009, with a power conversion efficiency (PCE) of 3.8% but only a few minutes of stability.[27] Conversely, the presence of Pb (a hazardous element in nature) in perovskite and concern regarding long-term stability are the biggest impediments to its commercialization.

To overcome these drawbacks and find a replacement for Pb, researchers have explored metal cations such as Sn^{2+} or Ge^{2+}, which are divalent and have a +2-level of oxidation and a similar configuration of the outermost shell that is comparable with Pb^{2+}.[28] The ionic radius of Sn^{2+} and Ge^{2+} is 1.35 Å and 0.73 Å, respectively, and that of Pb^{2+} is 1.49 Å. As a result, when Sn^{2+} and Ge^{2+} are used as divalent cations to substitute for Pb^{2+}, the perovskite crystal structure is not affected.[24,29] The oxidization of Sn^{2+} to Sn^{4+} occurs more easily because the Ge^{2+} ionic radius is less than that of Sn^{2+} and Pb^{2+}. Thus, Ge-based perovskite exhibits greater conductivity than Pb-based and Sn-based perovskite. According to the periodic table, a comparison of the alkali metals Rb and Cs indicates that the reactivity of Rb is lower than that of Cs (*i.e.*, Rb < Cs).[24]

Furthermore, $RbGeI_3$ possesses various promising properties such as a lower band gap of 1.31 eV, an electron affinity of 3.9 eV, a higher dielectric permittivity of 23.1 eV, and a higher electron and hole mobility of 28.6 $cm^2 V^{-1} s^{-1}$ and 27.3 $cm^2 V^{-1} s^{-1}$, respectively. Therefore, the choice of $RbGeI_3$ material as an absorber is much preferable.

In 1989, the thermometric characteristics of $RbGeI_3$ were explored *via* XRD and Raman spectroscopy by Theile *et al.*[30] In 2008, long-range-corrected density functional study for dye-sensitized solar cells was performed by Wong *et al.*[31] In 2019, different characteristics, including magnetic, electrical, and structural, of $RbGeI_3$-based (cubic) and rubidium dysprosium oxide ($RbDyO_3$-based) PSCs were explored by Khursheed *et al.*[32] In 2019, a first-principles study examining various characteristics, such as structural, electrical, and optical, of $RbGeI_3$-based PSCs was conducted, and several characteristics such as relative permittivity at static (ε_0), relative permittivity at high frequency (ε_∞), hole and electron effective masses (m_h^*, m_e^*), energy band gap, lattice parameters, and tolerance factor (0.90) were evaluated *via* the PBEsol function, as explored by Jong *et al.*[33] In 2021, Jayan *et al.* investigated the optoelectronic, thermoelectric, thermodynamic, mechanical, and structural properties of $RbGeI_3$-based (cubic $Pm\bar{3}m$ space group, three-dimensional structure) PSCs to determine different exchange correlation functions.[34] In 2022, Pindolia *et al.* researched the impact of various types of hole transport layers (HTLs) and electron transport layers (ETLs) on $RbGeI_3$ as the absorber layer.[25] In 2023, a theoretical maximum power conversion efficiency of 23.8% was achieved by Sarkar *et al.* through $RbGeI_3$ simulation using the solar cell capacitance simulator-one-dimensional (SCAPS-1D) simulator.[24]

One of the most popular techniques for *ab initio* calculations of atomic, molecular, crystallographic, and surface structures and their interactions is density functional theory (DFT). Also, the material's band gap, and electronic, magnetic, and optical properties can be estimated using DFT calculations. In 2024, a DFT study of $RbGeI_3$ was performed by Qin *et al.* to discover its excellent mechanical stability and resilience as well as its performance, which was evaluated using SCAPS-1D simulation software.[35] The novelty of this research includes the determination of a new structure with all inorganic materials through many trials with various layer configurations for enhancing the power conversion efficiency, and also the use of low-cost, non-toxic, earth-abundant materials for different layer materials.

In this study, $RbGeI_3$-based solar cells with various HTLs and ETLs were simulated to propose an improved cell structure and discuss the potential of this material. The properties of these materials are derived from previously published articles. The theoretical evolution of 19 different combinations was explored by incorporating ten inorganic HTMs ($BaSi_2$, $AgInTe_2$, Cu_2Te, CdSe, SnS, CuO, Sb_2Se_3, MoS_2, CuSCN, and Sb_2S_3), as well as ten inorganic ETMs (In_2S_3, In_3Se_4, CdS, WS_2, SnS_2, IGZO, ZnSe, In_2Se_3, $Cd_{0.5}Zn_{0.5}S$, and TiO_2) with the $RbGeI_3$-based absorber. After ascertaining the configurations with the greatest potential from 19 structures, we further investigated to optimize several properties such as temperature; work function of the left metal contact; series and shunt resistance; surface recombination velocity of electrons and holes; thickness of the perovskite-based absorber layer, ETM, and HTM; carrier concentration of the perovskite absorber layer, ETM, and HTM; defect density of the perovskite-based absorber layer, ETM, and HTM; and defect density at the interface of the HTL/absorber and absorber/ETL. Additionally, the *C–V* attribution and Mott–Schottky plot were also investigated. Finally, a comparison with earlier research was performed using the obtained solar cell parameters.

2. Simulation process, material specifications, and device-designing methodology

2.1 Simulation process and material specifications

The numerical simulation method is crucial for quickly comprehending the physical characteristics and functionality of PV devices as well as the behavior of each device parameter without expending a great deal of money and time. There are numerous simulation tools currently available, including PC1D, AFORS-HET, ATLAS, Sentaurus TCAD, AMPS-1D, wxAMPS, and SCAPS-1D, which are frequently utilized to build and assess a photovoltaic device's performance.[36–39] Notably, SCPAS-1D demonstrated significant potential for modeling and simulating various PV device structures with flexible parameters involving spectral response, carrier generation and recombination mechanism, capacitance and voltage relation, capacitance and frequency relation, working temperature, series resistance and

shunt resistance, metal contacts, and precisely calculated V_{oc}, J_{sc}, fill factor (FF), and PCE through numerical convergence and rapid single and batch calculations with an intuitive user interface.[24,40] Thus, the present investigation was conducted using the SCAPS-1D simulation tool.

Conversely, there are several restrictions on this tool. One of SCAPS-1D's restrictions is that it can only operate in one dimension. Additional drawbacks of the SCAPS-1D simulator are that it has a layer limit of seven, there is a volatile interpretation for a secondary barrier or n–p (rather than p–n) junction, and error in divergence occurs when the number of steps in simulation is limitless.[24,40] SCAPS-1D is a useful tool that was created by the Department of electronics and information systems (EIS) at the University of Gent in Belgium. Alex Niemegeers, Marc Burgelman, Koen Decock, Stefaan Degrave, and Johan Verschraegen are the researchers that have been involved in its development. The application was initially created for the $CuInSe_2$ and CdTe families of cell architectures.

At present, this program is also practicable for amorphous-type silicon (a-Si) cells, crystalline-type silicon (c-Si) SCs, and the GaAs family.[24,41–43] Additionally, SCAPS is a powerful tool for analyzing semiconductor equations (eqn (1)–(3)). By accounting for the boundary conditions, SCAPS-1D can solve Poisson's equation (eqn (1)), as well as the electron and hole continuity equations given in eqn (2) and (3), respectively, at every location within the device.[44–47] SCAPS-1D analyzes the operation of the photovoltaic devices by taking into account the Shockley–Read–Hall (SRH) recombination statistics:[42]

$$\frac{d^2}{dx^2}\{E(x)\} = \frac{e}{\varepsilon_0\varepsilon_r}\{p(x) - n(x) + N_D - N_A + \rho_p - \rho_n\} \quad (1)$$

where $E(x)$ denotes electrostatic potential; e denotes the charge of an electron; ε_0 and ε_r denote vacuum and relative permittivity, respectively; $n(x)$ and $p(x)$ denote the concentration of electrons and holes, respectively; N_A and N_D denote the charge density of acceptor and donor, respectively; and ρ_n and ρ_p denote the distribution of electrons and holes, respectively.

$$\frac{dJ_n}{dx} = G - R \quad (2)$$

$$\frac{dJ_p}{dx} = G - R \quad (3)$$

where J_n and J_p denote the electron and hole current density, respectively, and G and R denote the generation rate and recombination rate, respectively.

In semiconductors, carrier transport originates from drift and diffusion, and can be described as eqn (4) and (5).

$$J_n = D_n\frac{dn}{dx} + \mu_n n\frac{dE(x)}{dx} \quad (4)$$

$$J_p = D_p\frac{dp}{dx} + \mu_p p\frac{dE(x)}{dx} \quad (5)$$

where D_n and D_p denote the electron and hole diffusion coefficients, respectively, and μ_n and μ_p denote the electron and hole mobility, respectively. Table 1 shows the values of several specifications for separate layers of the proposed PSC device. Table 2 shows the value of defect density for different interfaces. Table 3 shows the values of various electrical characteristics for the front metal contact, as well as the back metal contact. Table 4 shows the values of various specifications for several HTL materials. Table 5 shows the values of various specifications for several ETL materials.

Table 1 Input specifications for the simulation of the proposed PSC device[a]

Specifications	ITO[42]	TiO_2[24]	$RbGeI_3$[24]	Sb_2S_3[44–46]
Thickness, L (nm)	50	10–100	100–1000	10–200
Bandgap, E_g (eV)	3.65	3.2	1.31	1.62
Electron affinity, χ (eV)	4	4	3.9	3.7
Dielectric permittivity (relative), ε_r (eV)	8.9	9	23.1	7.08
CB effective density of states, N_C (1 cm^{-3})	5.2×10^{18}	2.0×10^{18}	2.8×10^{19}	2.0×10^{19}
VB effective density of states, N_V (1 cm^{-3})	1×10^{18}	1.8×10^{19}	1.4×10^{19}	1×10^{19}
Electron thermal velocity, $v_{T,n}$ (cm s^{-1})	1×10^{7}	1×10^{7}	1×10^{7}	1.7×10^{7}
Hole thermal velocity, $v_{T,p}$ (cm s^{-1})	1×10^{7}	1×10^{7}	1×10^{7}	1.4×10^{7}
Electron mobility, μ_n (cm^2 V^{-1} s^{-1})	10	20	28.6	9.8
Hole mobility, μ_p (cm^2 V^{-1} s^{-1})	10	10	27.3	10
Shallow uniform donor density, N_D (1 cm^{-3})	1×10^{18}	10^{12}–10^{19}	—	—
Shallow uniform acceptor density, N_A (1 cm^{-3})	—	—	10^{12}–10^{21}	10^{12}–10^{21}
Defect type	Single acceptor	Single acceptor	Single donor	Single donor
Capture cross section (electrons), σ_n (cm^2)	1×10^{-15}	1×10^{-15}	1×10^{-15}	1×10^{-15}
Capture cross section (holes), σ_p (cm^2)	1×10^{-15}	1×10^{-15}	1×10^{-15}	1×10^{-15}
Energetic distribution	Uniform	Uniform	Uniform	Uniform
Energy level with respect to reference (eV)	0.600	0.600	0.600	0.600
Characteristic energy (eV)	0.100	0.100	0.100	0.100
Total defect density, N_t (1 cm^{-3})	1×10^{14}	10^{12}–10^{18}	10^{12}–10^{18}	10^{12}–10^{21}
Series resistance, R_s (Ω cm^2)	1			
Shunt resistance, R_{sh} (Ω cm^2)	1×10^{5}			

[a] N.B.: CB = conduction band, VB = valence band.

Table 2 Input specifications for the defect density of different interfaces

Specifications	$RbGeI_3/TiO_2$ interface	$Sb_2S_3/RbGeI_3$ interface
Defect type	Neutral	Neutral
Capture cross section (electrons), σ_n (cm^2)	1×10^{-19}	1×10^{-19}
Capture cross section (holes), σ_p (cm^2)	1×10^{-19}	1×10^{-19}
Energetic distribution	Single	Single
Energy level with respect to reference (eV)	0.600	0.600
Characteristic energy (eV)	0.100	0.100
Total defect density, n_t (1 cm^{-2})	10^{12}–10^{19}	10^{12}–10^{21}

2.2 Structure and design process for the device

PV device performance is generally evaluated by four performance specifications: J_{sc}, V_{oc}, FF, and PCE. The spectrum of the incident light (the global air mass 'AM1.5G, 1 Sun' spectrum at the temperature of 300 K was used in this investigation) and the optical characteristics (recombination, reflection, and absorption) affect the short circuit current density (J_{sc}). It can be evaluated using the formula in eqn (6):[59]

$$J_{sc} = q\sum_i T(\lambda)\frac{\pi_i(\lambda_i)}{h\nu_i}\eta_i(\lambda_i)\Delta\lambda_i \quad (6)$$

where q denotes the charge of an electron, $T(\lambda)$ indicates optical transmission, ϕ_i indicates spectral power density, and $\Delta\lambda_i$ indicates the interval between the two subsequent values of wavelength.

When there is no net current flowing through the solar cell, open circuit voltage (V_{oc}) is created and can be calculated using the formula in eqn (7):[60]

$$V_{oc} = \frac{nkT}{q}\ln\left(\frac{J_{sc}}{J_o} + 1\right) \quad (7)$$

where n, k, T, J_{sc}, and J_o denote the diode ideality factor, Boltzmann constant, ambient temperature, short circuit current density, and reverse bias saturation current density, respectively.

The solar cell's maximum power is determined by the fill factor (FF) and is stated in eqn (8):[61]

$$\mathrm{FF}\ (\%) = \frac{v_{oc} - \ln(v_{oc} + 0.72)}{v_{oc} + 1} \quad (8)$$

where $v_{oc} = \frac{q}{nkT}V_{oc}$ is denoted as normalized V_{oc}.

The efficiency for the photon's power conversion (PCE) is determined by eqn (9):[60]

$$\eta\ (\%) = \frac{V_{oc} \times J_{sc} \times \mathrm{FF}}{P_{in}} \quad (9)$$

Herein, P_{in} denotes the input photon's power from the sun (1000 W m^{-2} was used in this investigation).

To finalize the structure of a PV device, a study was performed to obtain additional information regarding the performance of the device with a combination of several HTLs and several ETLs. Unfortunately, charge transport materials (CTMs) consist of organic compounds that are very unstable.[62–65] Additionally, because of their simplest manufacturing technique, inorganic CTMs are inexpensive. Inorganic CTMs exhibit greater thermodynamical and chemical durability than organic CTMs. In comparison with organic CTMs, inorganic CTMs exhibit a wider band gap, greater mobility of the charge carrier, and superior transparency to the different radiations of visible, infrared, and ultraviolet.[66–69]

Therefore, in this investigation, to ascertain the primary structure of the PSC device, a PSC device based on inorganic $RbGeI_3$ was investigated by incorporating ten inorganic HTMs ($BaSi_2$, $AgInTe_2$, Cu_2Te, CdSe, SnS, CuO, Sb_2Se_3, MoS_2, CuSCN, Sb_2S_3) as well as ten inorganic ETMs (In_2S_3, In_3Se_4, CdS, WS_2, SnS_2, IGZO, ZnSe, In_2Se_3, $Cd_{0.5}Zn_{0.5}S$, TiO_2). The values of thickness and concentration of the charge carrier of the

Table 3 Input specifications for the front metal and back metal

Specifications	Front/right contact[48]	Back/left contact[49]
Material	Aluminum (Al)	Platinum (Pt)
Crystal lattice and orientation	FCC and 110	331
Surface recombination velocity of electrons (cm s^{-1})	1×10^7	1×10^5
Surface recombination velocity of holes (cm s^{-1})	1×10^5	1×10^7
Work function, Φ (eV)	4.06	5.12

Table 4 Input specifications for the simulation of several HTL materials

Specifications	$BaSi_2$[50]	$AgInTe_2$[17]	Cu_2Te[51]	CdSe[16]	SnS[52]	CuO[53]	Sb_2Se_3[16]	MoS_2[14,54]	CuSCN[25]
L (nm)	50	50	50	50	50	50	50	50	50
E_g (eV)	1.3	1.16	1.19	1.7	1.6	1.51	1.53	1.7	3.4
χ (eV)	3.3	3.6	4.1	3.93	3.6	4.07	4.04	3.8	1.7
ε_r (eV)	11.17	8.9	10	9.5	12.5	18.1	18	13.6	10
N_C (1 cm^{-3})	2.6×10^{19}	3.66×10^{19}	7.8×10^{17}	2.8×10^{19}	7.5×10^{18}	2.2×10^{19}	2.2×10^{18}	2.8×10^{19}	2.2×10^{19}
N_V (1 cm^{-3})	2×10^{19}	1.35×10^{19}	1.8×10^{19}	1.2×10^{19}	1.0×10^{19}	5.5×10^{20}	1.8×10^{19}	1×10^{19}	1.8×10^{18}
$\nu_{T,n}$ (cm s^{-1})	1×10^7	1×10^7	1×10^7	1×10^7	1×10^7	1×10^7	1×10^7	1×10^7	1×10^7
$\nu_{T,p}$ (cm s^{-1})	1×10^7	1×10^7	1×10^7	1×10^7	1×10^7	1×10^7	1×10^7	1×10^7	1×10^7
μ_n (cm^2 V^{-1} s^{-1})	820	1011	500	5.93	100	100	15	12	100
μ_p (cm^2 V^{-1} s^{-1})	100	887	100	25	4	0.1	5.1	2.8	25
N_A (1 cm^{-3})	1×10^{19}	1×10^{19}	1×10^{19}	1×10^{19}	1×10^{19}	1×10^{19}	1×10^{19}	1×10^{19}	1×10^{19}

Table 5 Input specifications for the simulation for several ETL materials

Specifications	In_2S_3[55]	In_3Se_4[56]	CdS[50]	WS_2[25]	SnS_2[57]	IGZO[25]	ZnSe[17]	In_2Se_3[58]	$Cd_{0.5}Zn_{0.5}S$[54]
L (nm)	50	50	50	50	50	50	50	50	50
E_g (eV)	2.8	1.8	2.42	1.87	2.24	3.05	2.7	2.4	2.8
χ (eV)	4.6	4.55	4.4	4.3	4.24	4.16	4.09	3.8	4
ε_r (eV)	13.5	5.54	10	11.9	10	10	10	10	10
N_C (1 cm^{-3})	2.2×10^{17}	1.0×10^{18}	2.2×10^{18}	2.4×10^{19}	2.2×10^{17}	5.0×10^{18}	1.5×10^{18}	2.2×10^{18}	1.0×10^{18}
N_V (1 cm^{-3})	1.8×10^{19}	1.0×10^{18}	1.8×10^{19}	1.0×10^{19}	1.8×10^{19}	5.0×10^{18}	1.8×10^{19}	1.8×10^{19}	1.0×10^{18}
$\nu_{T,n}$ (cm s^{-1})	1×10^7	1×10^7	1×10^7	1×10^7	1×10^7	1×10^7	1×10^7	1×10^7	1×10^7
$\nu_{T,p}$ (cm s^{-1})	1×10^7	1×10^7	1×10^7	1×10^7	1×10^7	1×10^7	1×10^7	1×10^7	1×10^7
μ_n (cm^2 V^{-1} s^{-1})	50	100	100	260	50	15	50	50	100
μ_p (cm^2 V^{-1} s^{-1})	20	50	25	51	50	0.1	20	12	25
N_A (1 cm^{-3})	1×10^{15}	1×10^{15}	1×10^{15}	1×10^{15}	1×10^{15}	1×10^{15}	1×10^{15}	1×10^{15}	1×10^{15}

Table 6 Recorded performance of the PSC device for different configurations through numerical simulation

Configuration	V_{oc} (V)	J_{sc} (mA cm^{-2})	FF (%)	PCE (%)
Al/ITO/TiO_2/$RbGeI_3$/$BaSi_2$/Pt	0.5915	32.115889	66.48	12.63
Al/ITO/TiO_2/$RbGeI_3$/$AgInTe_2$/Pt	0.7508	33.586818	71.52	18.04
Al/ITO/TiO_2/$RbGeI_3$/Cu_2Te/Pt	0.8468	34.061598	82.04	23.66
Al/ITO/TiO_2/$RbGeI_3$/CdSe/Pt	0.8976	34.091434	79.61	24.36
Al/ITO/TiO_2/$RbGeI_3$/SnS/Pt	0.8974	34.096428	81.29	24.87
Al/ITO/TiO_2/$RbGeI_3$/CuO/Pt	0.8918	34.105198	81.89	24.91
Al/ITO/TiO_2/$RbGeI_3$/Sb_2Se_3/Pt	0.9003	34.105396	81.78	25.11
Al/ITO/TiO_2/$RbGeI_3$/MoS_2/Pt	0.9003	34.097394	82.04	25.18
Al/ITO/TiO_2/$RbGeI_3$/CuSCN/Pt	0.8998	34.092787	82.10	25.19
Al/ITO/TiO_2/$RbGeI_3$/Sb_2S_3/Pt	**0.9002**	**34.100013**	**82.10**	**25.20**
Al/ITO/$Cd_{0.5}Zn_{0.5}S$/$RbGeI_3$/Sb_2S_3/Pt	0.8970	34.085439	81.21	24.83
Al/ITO/In_2Se_3/$RbGeI_3$/Sb_2S_3/Pt	0.8970	34.085248	80.88	24.73
Al/ITO/ZnSe/$RbGeI_3$/Sb_2S_3/Pt	0.8948	34.087093	80.95	24.69
Al/ITO/IGZO/$RbGeI_3$/Sb_2S_3/Pt	0.8715	34.089026	77.38	22.99
Al/ITO/SnS_2/$RbGeI_3$/Sb_2S_3/Pt	0.8717	34.088865	77.34	22.98
Al/ITO/WS_2/$RbGeI_3$/Sb_2S_3/Pt	0.7150	34.093955	71.79	17.50
Al/ITO/CdS/$RbGeI_3$/Sb_2S_3/Pt	0.6773	34.098321	70.81	16.35
Al/ITO/In_3Se_4/$RbGeI_3$/Sb_2S_3/Pt	0.5612	33.243283	42.62	7.95
Al/ITO/In_2S_3/$RbGeI_3$/Sb_2S_3/Pt	0.5424	3.074529	42.58	0.71

$RbGeI_3$-based absorber layer were initially set as 800 nm and 10^{16} cm^{-3} respectively, and that of each HTL as 50 nm and 1×10^{19} cm^{-3}, and each ETL as 50 nm and 1×10^{15} cm^{-3}, respectively, while other specifications remained the same as in Tables 1–3. Simulation was performed for different configurations with the combinations of various HTLs and ETLs, and all the primary data on performance parameters (such as V_{oc}, J_{sc}, FF, and PCE) were recorded.

Table 6 shows the data for four performance parameters, and the maximum device performance was obtained when Sb_2S_3 and TiO_2 were individually applied as HTM and ETM. Also, Sb_2S_3 possesses superior optoelectronic properties such as an appropriate band gap ($\sim$1.62 eV), a superior absorption coefficient ($\sim 10^5$ cm^{-1}), ingredient abundance on earth, minimal toxicity, and a low-cost production procedure.[52] Additionally, the valence band offset (VBO) of Sb_2S_3 and the conduction band offset (CBO) of TiO_2 are much lower in comparison with other HTLs and ETLs.

After numerous trials, the Al/ITO/TiO_2/$RbGeI_3$/Sb_2S_3/Pt structure proved to be an effective primary structure. Hence, further investigation, *i.e.*, optimization of several properties such as temperature; work function of the left metal contact; series and shunt resistance; surface recombination velocity of electrons and holes; thickness of the perovskite-based absorber layer, ETM, and HTM; carrier concentration of the perovskite absorber layer, ETM, and HTM; defect density of the perovskite-based absorber layer, ETM, and HTM; and defect density at the interface of HTL and the absorber layer, and also the absorber layer and ETL, were conducted with the structure of the PSC device as Al/ITO/TiO_2/$RbGeI_3$/Sb_2S_3/Pt.

2.3 Finalized structure of the device

Fig. 1(a) shows the finalized and optimized structure (Al/ITO/TiO_2/$RbGeI_3$/Sb_2S_3/Pt) of the proposed perovskite-based PV device. It was determined that p-type $RbGeI_3$ was the most attractive Pb-free, highly stable, efficient, and low-cost perovskite-based absorber material. On the top of the absorber, n-type TiO_2 ETL was used as a heterojunction associated with the $RbGeI_3$ absorber. It formed an n–p heterojunction interface that enhanced the collection of photogenerated electrons (PGEs) with blocking holes. On top of the TiO_2 layer, highly transparent, conductive, and low-cost n^+-type ITO was applied as a window layer. At the bottom of the absorber ($RbGeI_3$), a p^+-type Sb_2S_3 HTL was used to effectively collect photogenerated holes (PGHs) with blocking electrons that enhanced the overall efficiency of the proposed PSC. Aluminum (Al) was used as the front metal contact material, and platinum (Pt) was used as the back metal contact material. Fig. 1(b) shows the energy band diagram of the suggested device, which shows that there is a low VBO and adequately large CBO at the Sb_2S_3/$RbGeI_3$ interface, and the band configuration between Sb_2S_3 and $RbGeI_3$ is excellent for ensuring that hole transmission from the absorber as well as electron opposition are facilitated. Also, because of the adequately large VBO and very low CBO at the $RbGeI_3$/TiO_2 interface, the band configuration between $RbGeI_3$ and TiO_2 is excellent for ensuring smooth electron transmission from the absorber and facile hole opposition.

3. Results and discussion

3.1 Consequences of ETL thickness and carrier concentrations on the performance of the device and their optimization

There is considerable impact of the ETL's (TiO_2) carrier concentration as well as thickness on PSC performance, and they can

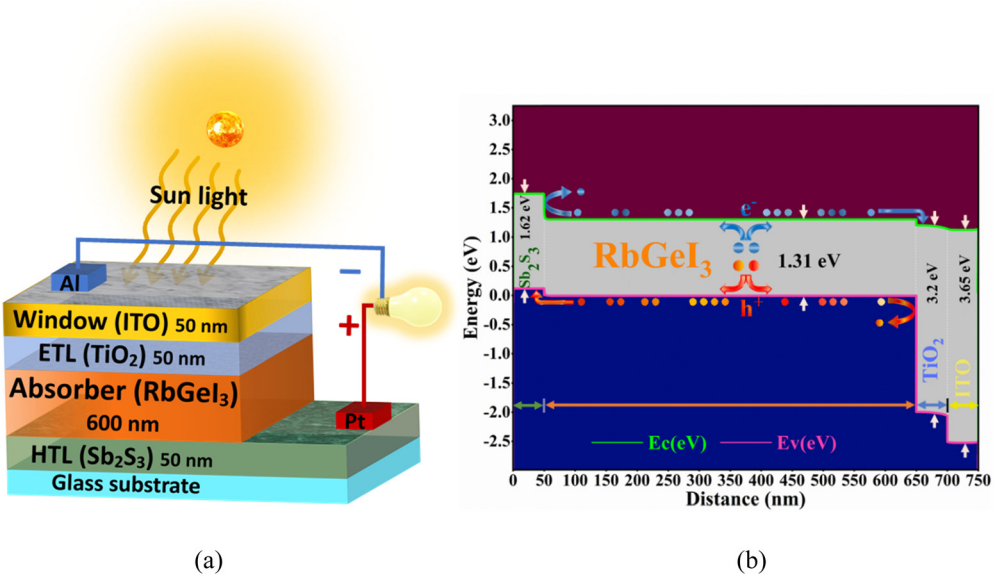

(a) (b)

Fig. 1 (a) Schematic diagram and (b) energy band diagram of the proposed PSC device.

be used to improve it. Therefore, when developing highly efficient PSCs, it is important to carefully select the ETL's characteristics. An optimal ETL for PSCs can assist in decreasing recombination currents and increasing transmittance.[70] In this investigation, the ETL's carrier concentration and thickness were varied consecutively within the range of 10^{12}–10^{19} cm^{-3} and 10–100 nm, while other specifications remained the same, as in Tables 1–3.

The variation in the device's performance according to the ETL's thickness is demonstrated in Fig. 2(a), which shows that all the PV performance parameters, *i.e.*, V_{oc}, J_{sc}, FF, and PCE, remain unchanged for 'with HTL' and 'without HTL.' All the PV parameters have a higher value 'with HTL' than 'without HTL.' Because there is no significant alteration in the PSC performance as the ETL's thickness is varied, 50 nm was selected as the optimal thickness for the ETL (TiO_2) layer to minimize fabrication costs.

The variation in the device's performance according to the ETL's carrier concentration is demonstrated in Fig. 2(b). Although there were lower values without HTL than with HTL

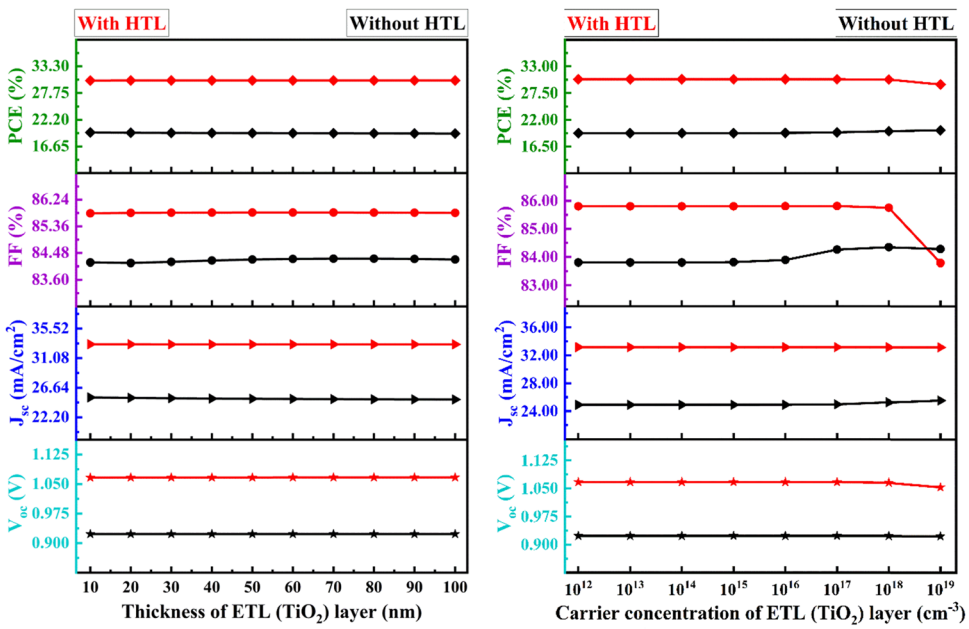

(a) (b)

Fig. 2 Consequences of the ETL (TiO_2) layer's (a) thickness and (b) carrier concentration on the device's performance.

for all the PV parameters, they remained nearly unchanged, except for FF as the carrier concentration, which was varied. The FF increased very slightly beyond 10^{16} cm^{-3}. Because this occurred as doping concentrations increased, they also raised the internal electric field of the ETL, thus increasing the transport velocity of the charge carriers and thereby conductivity.[71] The PV parameters have a higher value with HTL than without HTL, and they remained unchanged up to 10^{18} cm^{-3}. After that, V_{oc},J_{sc}, and PCE slightly decreased, but FF significantly decreased. The reason behind this is that coulomb traps resulted due to high doping concentrations, which in turn decreased the electron mobility.[72] Therefore, it was determined that the optimal carrier concentration for the ETL (TiO_2) layer was 10^{17} cm^{-3}.

3.2 Consequences of the absorber's thickness and carrier concentrations on the device's performance and their optimization

The perovskite layer's thickness and carrier concentration are critical elements for improving the PSC's performance, and they influence diffusion length, photocarrier generation, carrier lifetime, and extraction. As the absorber layer thickness increases, the generation and recombination rates of the carriers also increase.[73] In this investigation, the absorber layer's thickness and carrier concentration varied with the range (100–1000) nm and (10^{12}–10^{21}) cm^{-3} respectively, while other specifications remained the same as in Tables 1–3. The alteration in the device's performance according to absorber thickness is demonstrated in Fig. 3(a), where the open circuit voltage (V_{oc}) significantly increased up to 500 nm for the 'without HTL' configuration, and after that, it slightly increased. Although the V_{oc} for the 'with HTL' configuration is higher than that 'without HTL,' it slightly diminished with the initial increasing thickness. The reason behind this is that the recombination increases with the increase in absorber thickness, and hence the saturation current also increases.[72] The current density (J_{sc}) significantly increased up to 600 nm with the increase in thickness of the absorber layer. The significant increase in photon absorption is the primary cause of the rise of J_{sc}.[72] Beyond the 600 nm thickness of the absorber, the current density also increased, but not significantly in comparison. The reasons are that the photon absorption also increases, but not significantly, and the greater absorber layer influences charge carrier diffusion lengths, enhancing photogenerated carrier recombination *via* SRH recombination.[74] The fill factor (FF) for 'without HTL' significantly increased to 200 nm and that is in the opposite phase for "with HTL", and after that, the change in FF for both "with HTL" and "without HTL" is slight but in the opposite phase. In the case of "with HTL" structures, the reason for abrupt decreases in FF is that the series resistance (R_s) is growing as the thickness of the cell rises.[75,76] However, the FF is boosted in the 'with HTL' configuration rather than 'without HTL.' Because the PCE is determined by the parameters V_{oc}, J_{sc}, and FF as presented in eqn (9). Although V_{oc} and FF are slightly decreased for 'with HTL,' as a result of a significant increase in J_{sc} up to 600 nm thicknesses, the PCE significantly intensified up to 600 nm. The PCE (without HTL) increased due to the same reason but is lower than 'with HTL.' Therefore, it was determined that 600 nm was the optimal value of the thickness for the absorber ($RbGeI_3$), and this value was used to reduce fabrication costs.

The device's performance varied according to the absorber's carrier density, as demonstrated in Fig. 3(b). According to Fig. 3(b), the V_{oc} remained unchanged with an absorber carrier

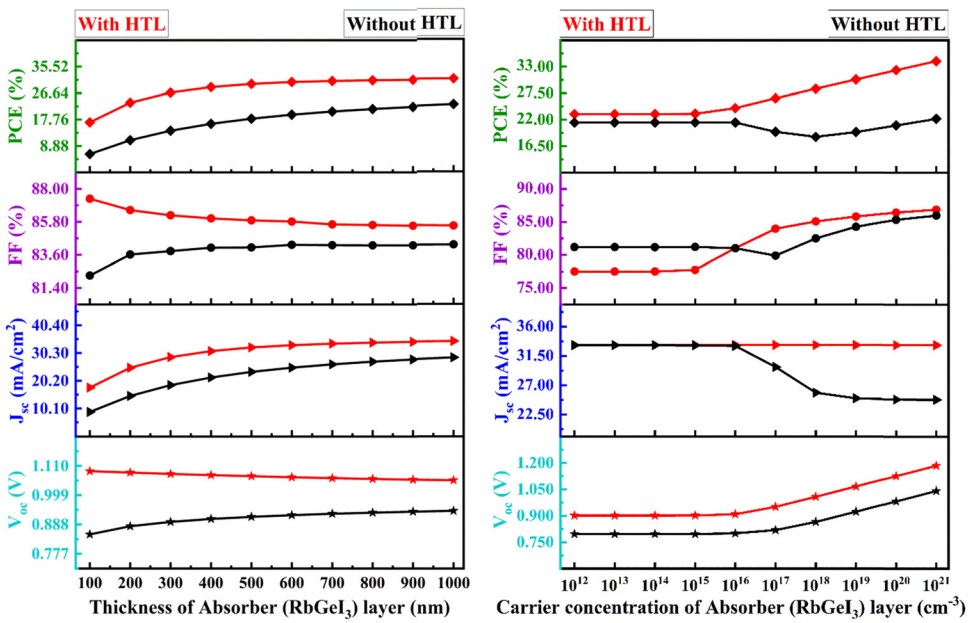

Fig. 3 Consequences of the absorber ($RbGeI_3$) layer's (a) thickness and (b) carrier density on the device's performance.

concentration of up to 10^{16} cm^{-3} for the 'with HTL' and 'without HTL' structures, and after that, it significantly increased. The key reason for this is because as the concentration of the carrier increases, the saturation current of the entire cell also increases, which reinforces the increase in V_{oc}.[21] Although the V_{oc} is lower for 'without HTL' than 'with HTL,' the J_{sc} remained unchanged with the variation of the carrier concentration for the 'with HTL'' structure. Thus, there is no substantial alteration of photon absorption within the variation of the carrier concentrations, and that is the principal reason for a lack of change in J_{sc}. The carrier concentration accelerates the recombination process by incorporating traps or recombination centers into the layer. At the front, the collection of the photogenerated carriers is then limited by this recombination process.[1,77] The increase in recombination rate may be the same as the increasing rate of J_{sc} due to the increase in carrier concentration, and hence, no significant change in J_{sc} occurred. However, for the 'without HTL' structure, the J_{sc} is the same as that for the 'with HTL' structure. Up to 10^{16} cm^{-3} and beyond that, it rapidly decreased up to 10^{18} cm^{-3}, and after that, it gradually decreased. This occurred because the recombination rate may be higher due to the rapid decrease in J_{sc}. The FF for the 'with HTL' configuration remained unchanged up to 10^{15} cm^{-3}, but after that, it significantly increased up to 10^{17} cm^{-3}, and beyond that, it slightly increased. The FF for 'without HTL' is less than that for the 'with HTL' configuration and remained unchanged up to 10^{16} cm^{-3}; after that, it slightly decreased up to 10^{17} cm^{-3}, and beyond that, it significantly increased. The fact behind this is that the increase in V_{oc} is due to an increase in carrier concentration. Because the PCE is determined by the parameters V_{oc}, J_{sc}, and FF, as presented in eqn (9), the J_{sc} remained unchanged for the 'with HTL' configuration, but as a result of a major increase in V_{oc} as well as FF, the PCE then significantly increased up to 10^{19} cm^{-3}. However, the PCE for 'without HTL' significantly decreased due to a considerable diminution of J_{sc}, although there was a slight increase in V_{oc} and FF. The optimal value of the carrier concentration for the absorber ($RbGeI_3$) layer was therefore taken as 10^{19} cm^{-3}.

3.3 Consequences of the HTL's thickness and carrier concentrations on device performance and their optimization

The HTL's (Sb_2S_3) thickness and the concentration of the carrier have the ability to greatly influence the PSC's performance, and can improve it. The HTL increased the SC effectiveness due to minimization of the surface recombination velocity (SRV) by producing a strong field near the rear electrode.[1] To examine the consequences of concurrent changes in thickness and concentration of the carrier of the HTL (Sb_2S_3) on the PSC device performance, a contour map was constructed with simultaneous variation of thickness and density of the carrier of the HTL (Sb_2S_3) within the range of 10–200 nm and 10^{14}–10^{21} cm^{-3}, respectively, while other specifications remained the same as in Tables 1–3. Fig. 4 illustrates the influence of simultaneous variation of thickness and concentration of the carrier of the HTL on the parameters that determine the performance of the PV devices.

According to Fig. 4(a), for the range of the variation of carrier density from 10^{14} cm^{-3} to 8×10^{20} cm^{-3}, the V_{oc} increased very negligibly within the increase of thickness for the range of 10 nm to 60 nm, and there was no alteration in the V_{oc} after 60 nm. Beyond 8×10^{20} cm^{-3}, the change in thickness did not considerably impact the V_{oc} of the proposed PSC device. Also, for a particular thickness, the V_{oc} was nearly unchanged for the range of 10^{14} cm^{-3} to 8×10^{20} cm^{-3}, and the V_{oc} slightly increased beyond 8×10^{20} cm^{-3}. The reason for this negligible increase in V_{oc} is that the Sb_2S_3 HTL produced an advanced built-in potential at the Sb_2S_3/$RbGeI_3$ interface,[56,78] as well as an increase in J_{sc}.[79]

Fig. 4(b) shows a very negligible increase in J_{sc} within the increase in thickness from 10 nm to 200 nm for the range of carrier concentrations of 10^{14} cm^{-3} to 8×10^{20} cm^{-3}, and the J_{sc} slightly increased beyond 8×10^{20} cm^{-3} within the increase in thickness. Also, for the range of thickness of 10–100 nm, J_{sc} was almost unchanged for the range of 10^{14} cm^{-3} to 8×10^{20} cm^{-3}, and for further than 8×10^{20} cm^{-3}, the J_{sc} slightly increased for the range of thickness of 100–200 nm. Photon absorption at longer wavelength spectra results in a slight increase in electron–hole pair generation through the tail-states-assisted (TSA) two-step photon upconversion process, which is the main reason for the slight increase in J_{sc}.[16,19,56]

According to Fig. 4(c), for the range of 10^{14} cm^{-3} to 8×10^{20} cm^{-3} for carrier concentration, the FF increased very negligibly within the increase in thickness for the range of 10 nm to 30 nm, and afterwards, the FF remained nearly unaffected. Beyond 8×10^{20} cm^{-3}, the variation in thickness had no impact on the FF of the proposed PSC device, and this occurred because V_{oc} has no impact on the thickness variation. Additionally, for a particular thickness, the FF was nearly unchanged from 10^{14} cm^{-3} to 8×10^{20} cm^{-3}. Away from 8×10^{20} cm^{-3}, the FF slightly increased because higher carrier concentrations reduced the series resistance of the cell, hence grading the FF of the cell.[80]

From Fig. 4(d), it is clear that the PCE increased very negligibly for the range of carrier concentrations from 10^{14} cm^{-3} to 8×10^{20} cm^{-3} within the increase in thickness for the range of 10 nm to 60 nm, and afterward, the PCE remained nearly unaffected. Beyond 8×10^{20} cm^{-3}, the variation in thickness had no impact on the conversion efficiency of the photon's power in the proposed PSC device. Additionally, for a particular thickness, the PCE was nearly unchanged for the range of 10^{14} cm^{-3} to 8×10^{20} cm^{-3}, and outside of 8×10^{20} cm^{-3}, the PCE slightly increased. This occurred because of all the combined effects of V_{oc}, J_{sc}, and FF.

Sb_2S_3 with a small thickness cannot offer a contact channel of low resistance, whereas increased layer thickness prevents carriers from transferring to an electrode. Hence, extending the length of diffusion and allowing recombination to occur *via* a trade-off may be considered to determine the optimal value of the HTL's thickness, which was determined to be 50 nm. Also, the reasons behind the increase in overall performance are that increased carrier concentration moves the Fermi level towards the valence band (VB), which accelerates the hole build-up at

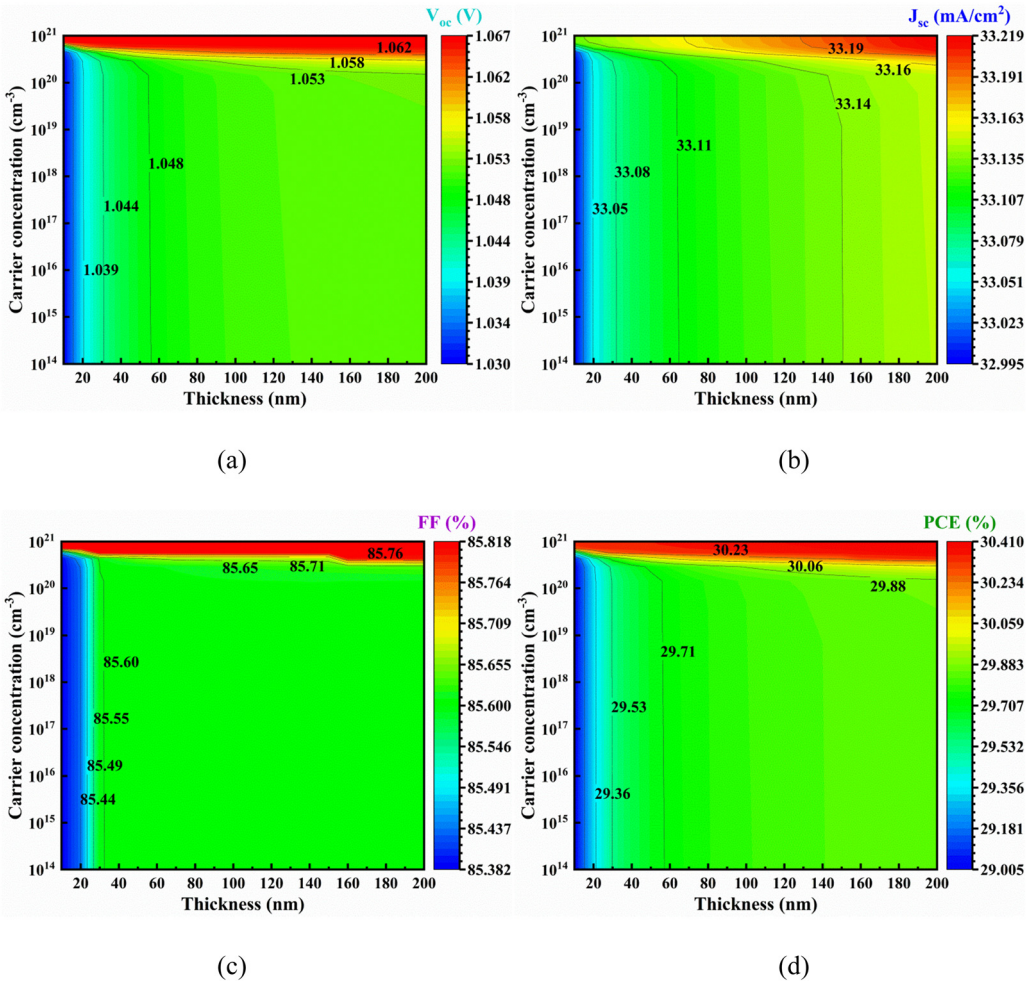

Fig. 4 Consequences to PV performance parameters (a) V_{oc}, (b) J_{sc}, (c) FF, and (d) PCE due to concurrent changes in thickness and density of the HTL carrier (Sb_2S_3).

the anode *via* creation of an ohmic contact with the rare metal contact,[81] and also due to increased carrier concentration. The HTL's internal electric field also increases, which implies a higher transport velocity for the charge carriers, and consequently, the conductivity.[72] The HTL's carrier concentration should be greater than the absorber layer's carrier concentration, and therefore, the optimal HTL carrier concentration was chosen as 10^{21} cm^{-3}.

3.4 Consequences of the bulk defect density of different layers on device performance and their optimization

3.4.1 In the case of the ETL (TiO_2). In this investigation, the density of bulk defect (N_t) of the single-acceptor type for the n-type ETL (TiO_2) was used. The defect density varied within the range of 10^{12}–10^{18} cm^{-3}, while other specifications remained the same, as in Tables 1–3. Fig. 5 illustrates the consequences of bulk defect density for the ETL, absorber, and HTL.

According to Fig. 5(a), for the 'with HTL' and 'without HTL' states, all the performance-determining parameters for the PV device, *i.e.*, V_{oc}, J_{sc}, FF, and PCE, were almost unchanged until 10^{17} cm^{-3}. After that, they significantly decreased, with the exclusion of V_{oc}. The density of bulk defect exhibits no influence on V_{oc}. However, all the PV performance parameters for 'with HTL' have a higher value as compared to 'without HTL.' The recombination rate of SRH increased due to the contribution of the TiO_2 layer's defect density, which lowered the SC's overall performance.[82] The optimal value of the bulk defect density was therefore taken as 10^{17} cm^{-3} for the best performance.

3.4.2 In the case of the absorber ($RbGeI_3$) layer. The construction of the device or the grade of the material's light-absorbing capacity has little effect on the PCE of the PSCs because photoelectrons are produced when the sun's light strikes the absorber layer. Poor morphology results from insufficient perovskite layer distribution on the ETL. Because of the reduced film excellence, the defect density is higher, which results in greater recombination.[76] In this investigation, the bulk defect density of the single-donor type for the p-type absorber ($RbGeI_3$) layer was used. The defect density varied within the range of 10^{12}–10^{18} cm^{-3}, and all other specifications remained the same, as in Tables 1–3. Fig. 5(b) illustrates the

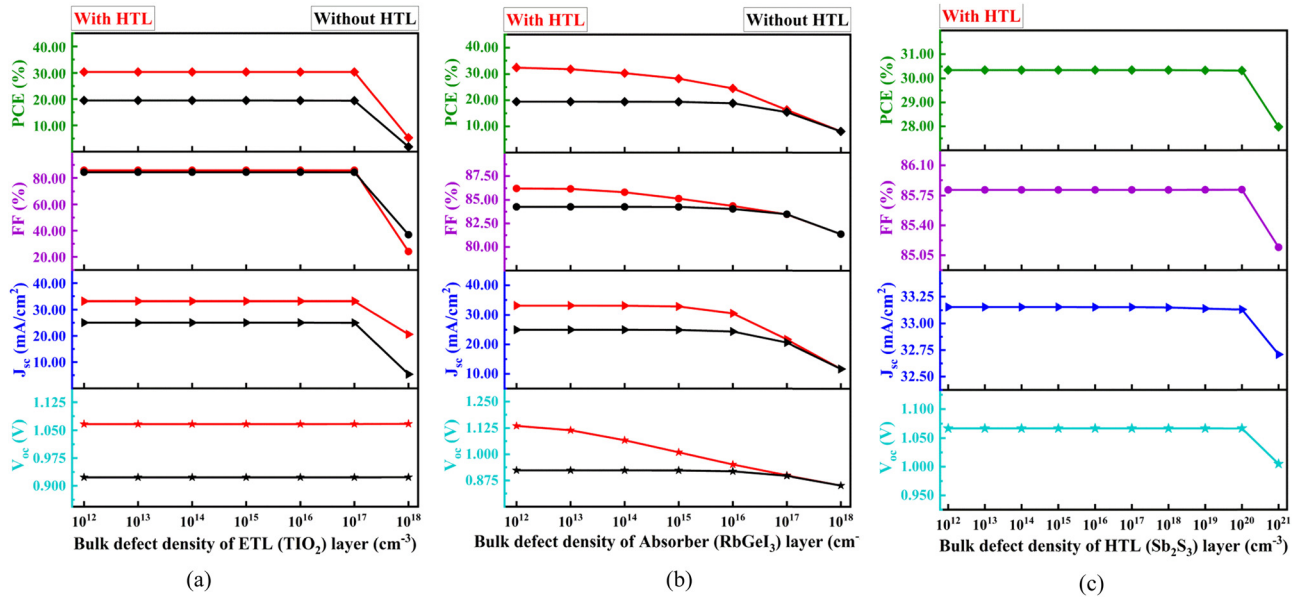

Fig. 5 Consequences of the bulk defect density of the (a) ETL (TiO_2), (b) absorber ($RbGeI_3$), and (c) HTL (Sb_2S_3) on the device performance.

consequences of the bulk defect density of the absorber layer on device performance.

According to Fig. 5(b), for the 'without HTL' configuration, all the performance-determining parameters of the PV device, *i.e.*, V_{oc}, J_{sc}, FF, and PCE, continued almost unchanged until 10^{16} cm^{-3}, and after that, they significantly decreased. For the 'with HTL' configuration, J_{sc} remained almost unchanged up to 10^{15} cm^{-3}, but after that, it significantly decreased up to 10^{16} cm^{-3}, and beyond that, it dramatically degraded. Initially, the V_{oc} slightly decreased to 10^{13} cm^{-3}, and beyond that, it sharply degraded. The FF and PCE significantly decreased at startup to 10^{16} cm^{-3}, and beyond that, they dramatically degraded. However, all the PV performance parameters for 'with HTL' had a higher value than that for 'without HTL.' The $RbGeI_3$ absorber layer's defect density enhances the recombination rate of SRH, which reduces the number of PGCs and thereby reduces the values of V_{oc}, J_{sc}, FF, and PCE.[83] The optimal value of the bulk defect density for the $RbGeI_3$ layer was therefore taken as 10^{14} cm^{-3} for best performance.

3.4.3 In the case of the HTL (Sb_2S_3). In this investigation, the bulk defect density of the single-donor type for the p$^+$-type HTL (Sb_2S_3) was used. The defect density varied within the range of 10^{12}–10^{21} cm^{-3}, and all other specifications remained the same, as in Tables 1–3. Fig. 5(c) illustrates the consequences of the bulk defect density of the HTL.

According to Fig. 5(c), all the performance-determining parameters of the PV device, *i.e.*, V_{oc}, J_{sc}, FF, and PCE, were strictly unchanged until 10^{20} cm^{-3} within the variation of the bulk defect density, and beyond that, they sharply decreased. This implies that there was no influence of the HTL's defect density up to 10^{20} cm^{-3} on the performance of the proposed PSC. The optimal value of the bulk defect density of the HTL was therefore taken as 10^{14} cm^{-3} for best performance.

3.5 Consequences of defect densities at different interfaces on the performance of the device and their optimization

3.5.1 In the case of the absorber/ETL interface. In the heterojunction PV device, an interfacial defect develops during the fabrication process as a result of various structural imperfections. This implies that testing the consequences of interfacial imperfections on SC properties is urgent. To replicate more realistic conditions in this investigation, the interfacial defect (n_t) of neutral type for the absorber/ETL interface was added. The defect density varied within the range of 10^{10}–10^{18} cm^{-2}, and all other specifications remained the same, as in Tables 1–3. Fig. 6 exemplifies the consequences of the defect density of the interface.

According to Fig. 6(a), for the 'without HTL' configuration, all the performance-determining parameters of the PV device, *i.e.*, V_{oc}, J_{sc}, FF, and PCE, were almost unchanged until 10^{16} cm^{-2}; after that, they significantly decreased. For the 'with HTL' condition, J_{sc} and FF remained almost unchanged up to 10^{16} cm^{-2}, and after that, they significantly decreased. Initially, the V_{oc} slightly decreased to 10^{13} cm^{-2}, and beyond that, it sharply degraded. The PCE remained almost unchanged up to 10^{13} cm^{-2}, but after that, it significantly decreased up to 10^{16} cm^{-2}, and beyond that, it dramatically degraded. The diminution in device performance could be due to the increase in defect density at the interface of the absorber/ETL. Also, electrons have a greater risk of being trapped, dispersed, or recombined while traveling from the absorber to the ETL, which reduces the charge carriers produced by the photon and hinders the accumulation of carriers.[84] However, all the performance-determining parameters of the PV device for the 'with HTL' configuration have a higher value as compared to those 'without HTL.' The V_{oc} is significantly more sensitive to n_t than J_{sc}, and the n_t range was preferred to 10^{12} cm^{-2} for V_{oc}.

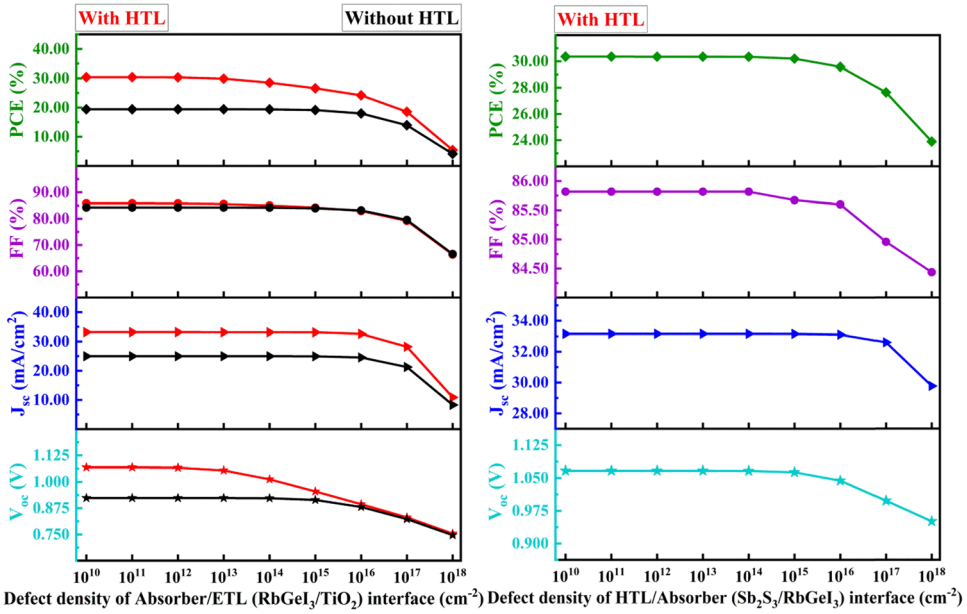

Fig. 6 Consequences of the defect at the (a) absorber ($RbGeI_3$)/ETL (TiO_2) and (b) HTL (Sb_2S_3)/absorber ($RbGeI_3$) interface on the device performance.

The interface recombination V_{oc} limit may be calculated using the formula in eqn (10):[85]

$$V_{oc} = \frac{1}{q}\left\{\phi_c - AkT\ln\left(\frac{qN_V S_t}{J_{sc}}\right)\right\} \quad (10)$$

where S_t denotes interface recombination velocity, A symbolizes the ideality factor of the hetero-junction, k symbolizes the Boltzmann constant, and ϕ_c denotes an effective barrier height.

3.5.2 In the case of the HTL/absorber interface. To replicate more realistic conditions in this investigation, an interfacial defect density of neutral type for the HTL/absorber interface was added. The defect density varied within the range of 10^{10}–10^{18} cm^{-2}, while other specifications remained the same, as in Tables 1–3. Fig. 6(b) illustrates the consequences of interface defect density.

According to Fig. 6(b), for the 'with HTL' configuration, all the performance-determining parameters of the PV device, *i.e.*, V_{oc}, J_{sc}, FF, and PCE, continued almost unchanged until 10^{15} cm^{-2}, excluding J_{sc}, which remained unchanged up to 10^{16} cm^{-2}, and beyond that, it significantly decreased. The reason behind this is similar to that explained earlier in the above section. Therefore, the optimal density of the interface defect for the HTL/absorber interface was chosen at 10^{12} cm^{-2}.

3.6 Consequences of different resistances on device performance and their optimization

The electrical resistances in the PSCs are introduced by the metal contacts used as front and back contacts in the perovskite absorbers, HTLs, and ETLs. The series (R_s) and shunt (R_{sh}) resistances play a key role in influencing the PV characteristics of SCs. Therefore, it is obligatory to understand the impacts of R_s and R_{sh} to improve the cell function. The Shockley equations determine the J–V properties of SCs when considering ideal one-sun illumination conditions, as in eqn (11) and (12).[86,87]

$$J_{sc} = J_{ph} - J_o\left[e^{\left\{\frac{q(V+J_{sc}R_s)}{AkT}\right\}} - 1\right] - \frac{V + J_{sc}R_s}{R_{sh}} \quad (11)$$

where q, A, k, T, J_{sc}, J_{ph}, J_o, V, R_s, and R_{sh} denote the elementary charge, ideality factor of the heterojunction, Boltzmann constant, ambient temperature, short circuit current density, photo-irradiated constant current density, reverse bias saturation current density, output voltage, and series and shunt resistances, respectively.

Because of an open-circuit condition, *i.e.*, $J_{sc} \approx 0$ mA cm^{-2}, V_{oc} is denoted as follows:

$$V_{oc} = R_{sh}\left[J_{ph} - J_o\left\{e^{\left(\frac{qV_{oc}}{AkT}\right)} - 1\right\}\right] \quad (12)$$

3.6.1 In the case of series resistance. In this investigation, series resistance variation was conducted in the range of (0–10) Ω cm^2 to study the influence on the PV performance parameters, while other specifications remained the same, as in Tables 1–3. Fig. 7(a) illustrates the consequences of series resistance, and shows that for the 'with HTL' and 'without HTL' configurations, the series resistance has no effect on J_{sc} and V_{oc}, but has a greater impact on FF and PCE. It is evident from the figure that FF significantly decreases from the beginning of the variation of R_s, and thereby PCE as well, which occurred because the increased series resistance accelerated the power loss. However, all the PV performance parameters

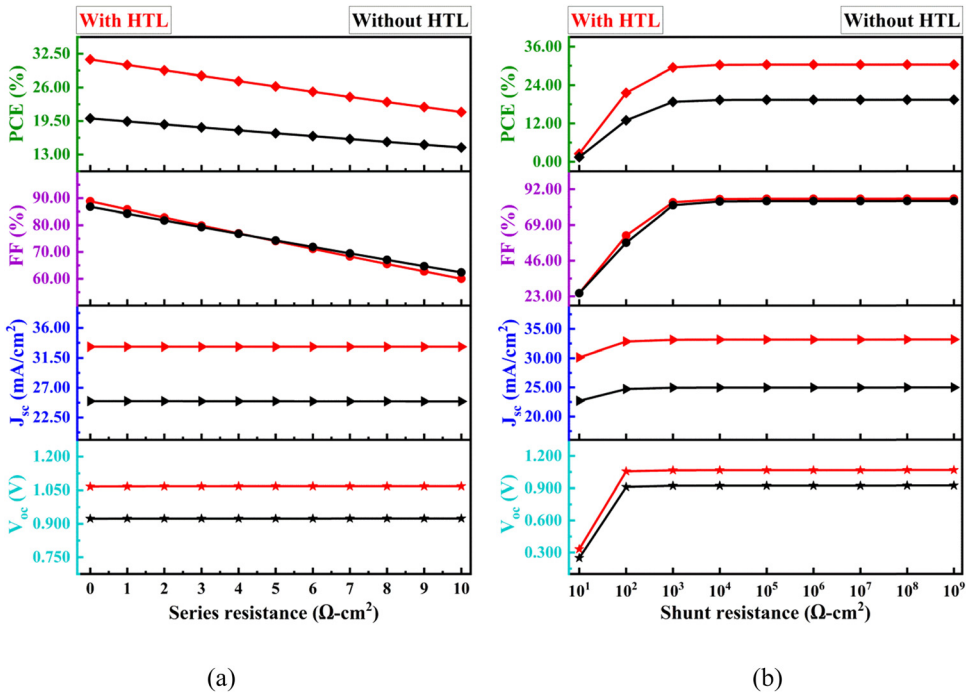

Fig. 7 Consequences of (a) series resistance (R_s) and (b) shunt resistance (R_{sh}) on device performance.

for 'with HTL,' excluding FF, have a higher value as compared to 'without HTL.' Andriessen and colleagues found that the increased series resistance of electrodes caused a greater loss of conversion efficiency in PSC devices once the active regions were augmented.[88] Although there are limitations to reducing series resistance due to the fabrication process and material's inherent properties, the optimal series resistance for the proposed PSC was chosen as 1 Ω cm^2.

3.6.2 In the case of shunt resistance. Shunt resistance was introduced by several charge recombination routes in the PSC.[72] In this investigation, the shunt resistance was varied within the range of 10^1–10^9 Ω cm^2 to study its influence on the PV performance parameters, while other specifications remained the same, as in Tables 1–3. Fig. 7(b) illustrates the consequences of shunt resistance, and shows that for the 'with HTL' and 'without HTL' configuration, the J_{sc} and V_{oc} sharply increase up to 10^2 Ω cm^2, and beyond that, the shunt resistance has no effect on J_{sc} or V_{oc}. It is also evident from the figure that the FF and PCE significantly increase from the beginning of the variation up to 10^3 Ω cm^2, and after that, they remain strictly unchanged. The reason behind the grading in cell performance is that the increase in shunt resistance degrades current loss. For the proposed PSC, 10^5 Ω cm^2 was chosen as the optimal shunt resistance.

3.7 Consequences of surface recombination velocity (SRV) on device performance and its optimization

The consequences of SRV at the back metal contact on the performance-determining parameters of the planned PSC device were thoroughly investigated, as seen in Fig. 8.

3.7.1 In the case of the electron's SRV. The SRV of electrons varied within the range of 10^1–10^{10} cm s^{-1}, while other specifications remained the same, as in Tables 1–3. The influence on the performance-determining parameters by reason of the variation of electron SRV is illustrated in Fig. 8(a). According to Fig. 8(a), for the 'without HTL' configuration, all the performance-determining parameters for the PV device, *i.e.*, V_{oc}, J_{sc}, FF, and PCE, significantly degraded until 10^4 cm s^{-1}. After that, there was no impact of electron SRV on the performance parameters. Before reaching metal contact, electron and hole recombination occurred with greater SRV, which implied a significant decrease in performance parameters. This drawback may be overcome by adding an HTL, which is visible in Fig. 8(a). This figure shows the evidence that there is no effect of electron SRV on the performance parameters for the 'with HTL' structure. Although the electrons have a higher SRV, they are prevented by the HTL from attaining back metal contact, and thus no electron–hole recombination occurs, resulting in no limitation on performance parameters.

3.7.2 In the case of the hole's SRV. The SRV of holes varied within the range of 10^1–10^{10} cm s^{-1}, while other specifications remained the same, as in Tables 1–3. Fig. 8(b) illustrates the influence on the performance-determining parameters by reason of the variation of hole SRV. According to Fig. 8(b), for the 'without HTL' configuration, all the performance-determining parameters of the PV device, *i.e.*, V_{oc}, J_{sc}, FF, and PCE, remain unchanged with the variation in the hole's SRV. However, for the 'with HTL' configuration, although there is no influence of hole SRV variation on J_{sc} and V_{oc}, the FF significantly increased up to 10^3 cm s^{-1}, and beyond that, it remained unchanged, which implies enhancement of the PCE. This occurred because holes are accelerated by

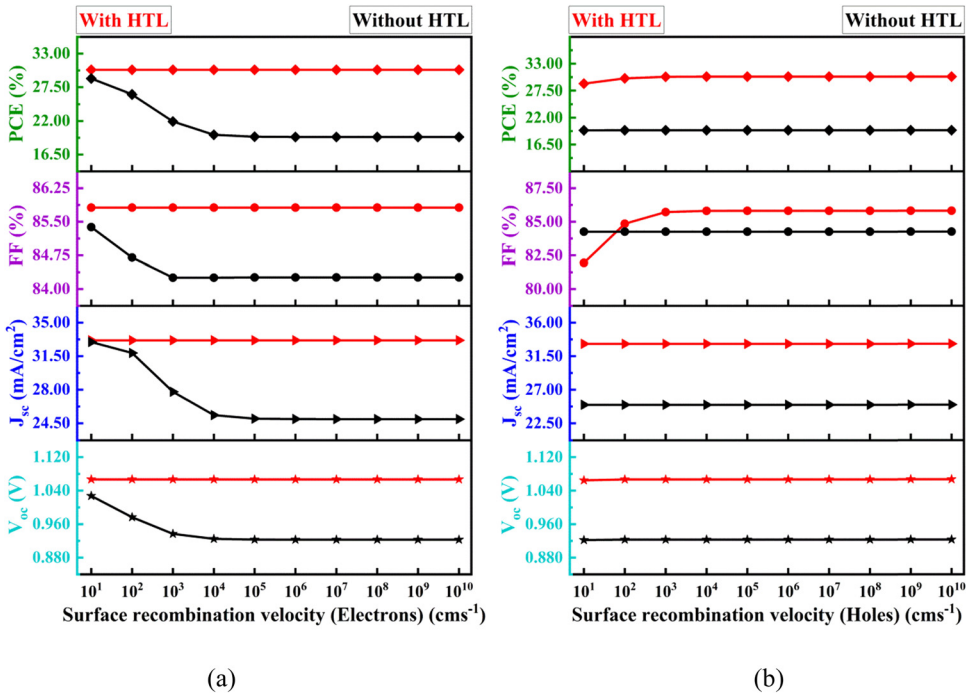

Fig. 8 Consequence of the surface recombination velocity of (a) electrons and (b) holes on device performance.

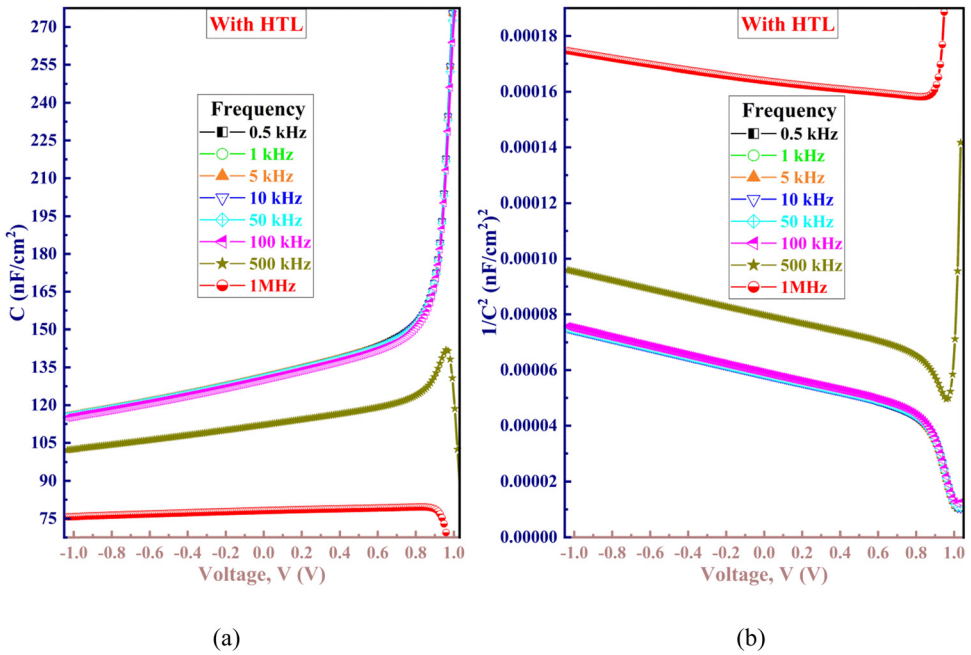

Fig. 9 (a) C–V attribution curve and (b) $(1/C^2) - V$ (Mott–Schottky plot) curve of the device.

the HTL and do not attain back metal contact, which thereby enhances the FF and PCE of the proposed PSC device.

3.8 C–V attribution and Mott–Schottky plot analysis of the device

3.8.1 Inspection of the C–V attribution and Mott–Schottky plot. Capacitance–voltage (C–V) inspections were conducted at different frequencies, *i.e.*, within the range of 0.5 kHz to 1 MHz, while other specifications remained the same, as in Tables 1–3, by applying the DC bias potential difference, as depicted in Fig. 9(a). The net capacitance generally appears from the depletion as well as diffusion capacitances linked with the p–n junctions for all the PV devices.

The depletion capacitance, *i.e.*, space charge capacitance, appeared by reason of the reverse bias condition in the

depletion region and in a similar manner to that of the parallel plate capacitor, whose capacitance is given by eqn (13):[89]

$$C_{\mathrm{dl}} = \frac{\varepsilon A}{W} \tag{13}$$

where, ε, A, and W denote the permittivity of the material, the area of the SC, and depletion width at the junction interface, respectively.

Conversely, the capacitance formed by diffusion appeared per unit area due to the forward bias condition, and this capacitance can be given by eqn (14):[90]

$$C_{\mathrm{dff}} = \frac{q^2 L n_0}{kT} \exp\left(\frac{qV_{\mathrm{F}}}{\eta kT}\right) \tag{14}$$

where q denotes the absolute value of electronic charge, L denotes the layer's thickness for the accumulation of charge, n_0 denotes the concentration of the minority carrier at equilibrium, η denotes the diode ideality factor, k denotes the Boltzmann constant, and T denotes the absolute temperature.

According to Fig. 9(a), the capacitance of the proposed PSC was nearly 78 nF cm^{-2} at zero bias. Two regions are specified: the first region within the range of −1.0 V to 0.7 V implies that the capacitance linearly changes with a particular slope for all frequencies, whereas the second region beyond 0.7 V implies that the capacitance exponentially increases for all frequencies, excluding 1 MHz, which has the same slope as before. The exponential nature of the capacitance is similar to that of the previous study.[90] It is also evident from the figure that the capacitance decreases at a particular bias potential with an increase in frequency, and then rises at a particular frequency with an increase in bias potential. Because of the insensitivity of absorber traps at higher frequencies, traps functionally do not respond and lower the functional charge to ensure decreased capacitance ($C = Q/V$) of the device. A noticeable trap in the figure is that the capacitance of the device is almost insensitive to the bias voltage at the frequency in the visible range.

Mott–Schottky (MS) plots are a renowned and reliable tool for determining the built-in potential (V_{bi}) of the variance between an electrode's work functions[91] and a device's carrier concentration level. Fig. 9(b) describes the MS plot at different frequencies for the proposed PSC device. The flat band potential at the interface is an essential characteristic of SC design. The charge carrier transmission at the interface is facilitated by the larger flat-band potential. The SC's flat-band potential results from the joining point of the $1/C^2$ curve and the voltage axis in the MS plot. According to Fig. 9(b), the slope of each curve for different frequencies is negative, and all are linear in nature. This implies that holes are the majority carriers, and the space-charge region occupies the majority of the p-type $RbGeI_3$ layer.[1] Additionally, the linear section of the MS curves across all observed frequencies exhibits an essentially constant slope. Conversely, for these observed frequencies, the intersection of each linear region at $1/C^2 = 0$ is different. The localized deep states in the absorber material might be the cause of this deviation, according to certain theories. The deep state contribution is negligible at higher frequencies, and the majority of the capacitance contribution is derived from the inflection of majority carriers near to the depletion region's boundary.[92]

3.8.2 Consequences of the thickness and concentration of the carrier of the absorber layer on the *C–V* attribution. To investigate the consequences of thickness and concentration of the carrier of the absorber layer on the *C–V* attribution, the thickness as well as carrier density of the absorber layer were varied within the range of 300–900 nm and 10^{14}–10^{19} cm^{-3}, respectively, while other specifications remained the same, as in Tables 1–3, at a constant frequency of 1 MHz. According to Fig. 10(a), the capacitance of the device linearly increases with nearly constant slope for all thicknesses within the variation of the bias potential. Also, the figure depicts that the change in capacitance with the variation in thickness is insignificant, and these results were also obtained in a previous study.[93]

Also, according to Fig. 10(b), the capacitance of the device increases with the rise in bias potential for all carrier concentrations and acts as an MS junction. The figure also shows that at a fixed bias potential, the capacitance dramatically increases with the carrier concentration. The increase in doping density increases the charge buildup at the interface, which implies an increase in capacitance, as reported in a prior study.[1]

3.9 Consequences of the back metal contact work function on device performance and its optimization

The back metal contact's work function exerts a crucial influence on the PSC's stability and performance. To gather holes from the external circuit on the HTM layer, an electrode of metal is situated. Making contact with an ohmic type is a prerequisite for the suitable assemblage of the charge of the majority carrier, *i.e.*, a hole through the contact of the back metal. In this investigation, to study the consequence of the work function of the back metal on the performance-determining parameters of PV devices, ten back metal work functions were used (5.00 eV (C, Co, Ge, Ir), 5.04 eV (Ni), 5.12 eV (Pt), 5.22 eV (Ni, Pd, Pt, W), 5.31 eV (Au), 5.35 eV (Ni), 5.37 eV (Au), 5.42 eV (Ir), 5.47 eV (Au), and 5.60 eV (Pd)),[48,49,94] while other specifications remained the same, as in Tables 1–3. Fig. 11(a) illustrates the influence of alteration of the back metal work function on the performance-determining parameters of the PV devices. For the 'without HTL' structure, all the performance-determining parameters of the PV device, *i.e.*, V_{oc}, J_{sc}, FF, and PCE, remained almost unchanged until 5.22 eV. After that, they substantially increased to 5.42 eV, and beyond that, they again remained unchanged. The greater the metal's work function for the back contact, the lower the barrier height, and therefore, from the absorber, the transmission of holes becomes smoother. Consequently, cell efficiency has been substantially increased.[52] The figure also shows that there is no consequence of the back metal work function on the device's performance for the 'with HTL' structure. Hence, a suitable back metal, Pt (5.22 eV), was used in this investigation.

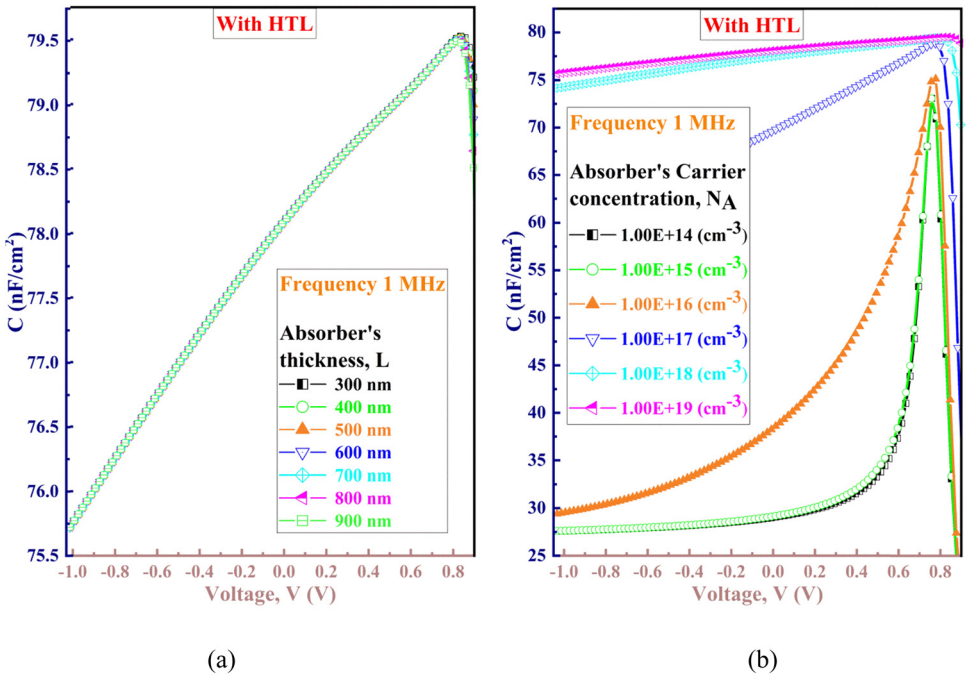

Fig. 10 The effect of the absorber ($RbGeI_3$) layer's (a) thickness and (b) concentration of the carrier on the *C*–*V* curve of the device.

3.10 Consequences of temperature on device performance

Temperature crucially impacts the PSC's stability and performance. In this investigation, real environmental conditions were used to study the impact of temperature on the performance-determining parameters of the PV devices and the stability of the proposed PSC device. The temperature was varied within the range of 280–500 K, while other specifications remained the same, as in Tables 1–3. The influence on the performance value due to the alteration of the temperature is demonstrated in Fig. 11(b). According to the figure, for 'with HTL' and 'without HTL,' except for J_{sc}, all the performance parameters of the PV device, *i.e.*, V_{oc}, FF, and PCE, significantly decreased from the initiation of the temperature variation. More electron–hole pairs were formed with the increase in temperature, which implies

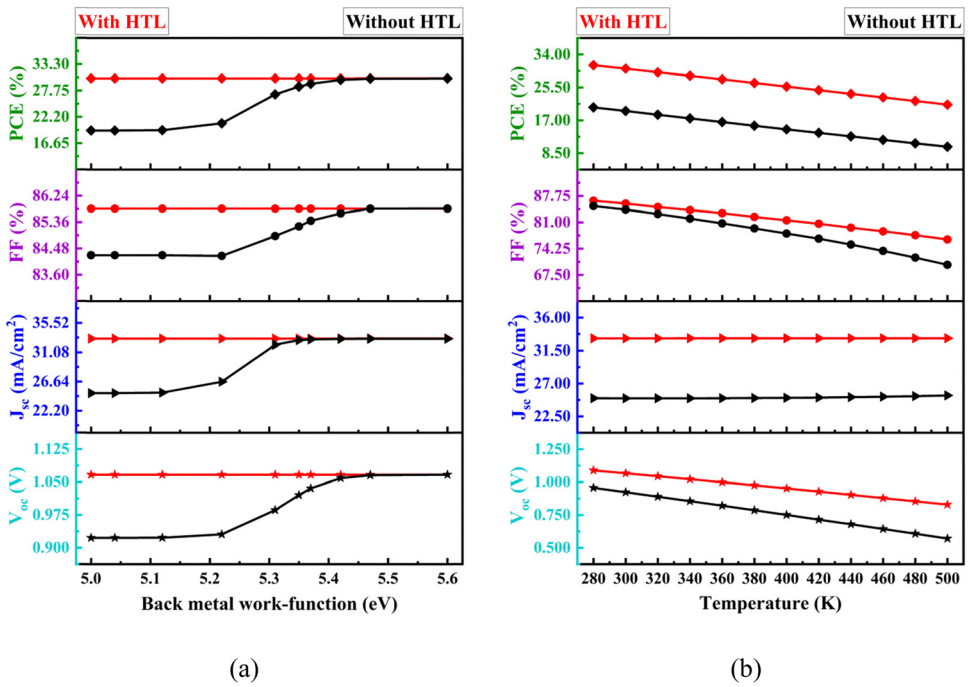

Fig. 11 Consequences of the (a) back metal work function (Φ) and (b) temperature (T) on device performance.

increasing recombination rates between energy bands. The reverse saturation current was increased by the carrier's internal recombination rate, which lowered the V_{oc},[95] and it can be realized by eqn (7). In addition, raising the temperature increased interface defects, which may be responsible for lowering V_{oc}. When the temperature was increased, the FF and PCE values decreased, which was probably due to a decrease in the shunt resistance.[96] However, all the PV performance parameters 'with HTL' have a higher value as compared to 'without HTL.' Fig. 11(b) recommends that to chose at room temperature (300 K) of the proposed PSC device with HTL.

3.11 Optimized features of the proposed PSC device

3.11.1 Justification of the appropriateness of Sb_2S_3 and TiO_2 as HTLs and ETLs, respectively. A diagram of the energy state for the perovskite absorber layer, different HTLs and ETLs, as well as back and front contacts, are shown in Fig. 12. The band alignment in the heterojunction solar cell layers, specifically, the conduction band offset (CBO) at the interface of the ETL and absorber layers as well as the valence band offset (VBO) at the interface of the absorber and HTLs, are the main determinants of the collection efficiency for the photogenerated carrier.[97] Using eqn (15) and (16),[97] the CBO and VBO at the ETL/absorber and absorber/HTL interfaces for different HTLs and ETLs were calculated, and are tabulated in Table 7.

$$\mathrm{CBO} = \chi_{\mathrm{absorber}} - \chi_{\mathrm{ETL}} \quad (15)$$

$$\mathrm{VBO} = (\chi_{\mathrm{ETL}} - \chi_{\mathrm{absorber}}) + (E_{\mathrm{g(HTL)}} - \chi_{\mathrm{g(Absorber)}}) \quad (16)$$

where χ_{absorber}, χ_{ETL}, and χ_{HTL} denote the electron affinity of the three layers, *i.e.*, absorber, ETL, and HTL materials, respectively. Also, $\chi_{\mathrm{g(Absorber)}}$ and $E_{\mathrm{g(HTL)}}$ denote the bandgap of absorber and HTL materials, respectively.

A larger negative or positive value of VBO promotes hole accumulation at the HTL/absorber interface, which results in a higher rate of recombination at the interface, and hence, the SC performance will be degraded. Therefore, a lower negative or positive VBO should have been expected. Again, the transit of holes generated by photons from the layer of absorbers to the HTLs is hindered by positive VBO, whereas when negative VBO is considered, no such type of hindrance occurred.[98]

Table 7 VBO and CBO of different HTMs and ETMs

Different layers	VBO (eV)	CBO (eV)
$BaSi_2$ (HTL)	+0.61	+0.60
$AgInTe_2$ (HTL)	+0.45	+0.30
Cu_2Te (HTL)	−0.08	−0.20
CdSe (HTL)	−0.42	−0.03
SnS (HTL)	+0.01	+0.30
CuO (HTL)	−0.37	−0.17
Sb_2Se_3 (HTL)	−0.36	−0.14
MoS_2 (HTL)	−0.29	+0.10
CuSCN (HTL)	+0.11	+2.20
Sb_2S_3 (HTL)	**−0.11**	+0.20
TiO_2 (ETL)	−1.99	**−0.10**
$Cd_{0.5}Zn_{0.5}S$ (ETL)	−1.59	−0.10
In_2Se_3 (ETL)	−0.99	+0.10
ZnSe (ETL)	−1.58	−0.19
IGZO (ETL)	−1.27	−0.34
SnS_2 (ETL)	−2.00	−0.26
WS_2 (ETL)	−0.96	−0.40
CdS (ETL)	−1.61	−0.50
In_3Se_4 (ETL)	−1.14	−0.65
In_2S_3 (ETL)	−2.19	−0.10

From the table, it is evident that there are lower negative VBOs of −0.08 eV and −0.11 eV for Cu_2Te and Sb_2S_3, respectively, and thus, Cu_2Te is more acceptable as an HTL material because if VBO is negative, there is no barrier preventing the photogenerated holes from moving toward the back electrode. Also, interface recombination increases as a result of an increase in negative VBO.[98] However, according to Table 6, the PCE of Cu_2Te is lower than that of Sb_2S_3. Therefore, Sb_2S_3 may be realized as an appropriate HTL material.

Also, a larger negative CBO value promotes electron accumulation at the absorber/ETL interface, resulting in a higher rate of recombination at the interface, and hence, the SC performance will be degraded. Therefore, a lower negative CBO should have been expected. Again, the transit of electrons generated by the photons from the absorber towards the ETLs

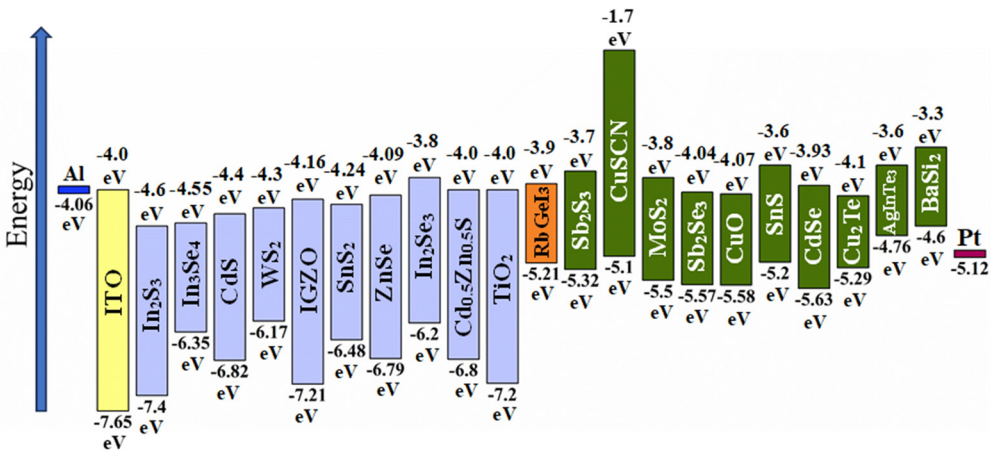

Fig. 12 Energy band for perovskite absorber, and different HTMs and ETMs, as well as back and front contacts.

is hindered by a positive CBO, whereas there is no such type of hindrance for a negative CBO.[98] From Table 7, it is also evident that TiO_2, $Cd_{0.5}Zn_{0.5}S$, and In_2S_3 have a lower negative CBO of −0.10 eV. However, according to Table 6, the PCE of TiO_2 is higher than that of other ETLs. Therefore, we chose TiO_2 as an appropriate ETL material.

3.11.2 QE *vs.* wavelength and *J vs. V* characteristics. Fig. 13(a) and (b) demonstrate the QE-wavelength and *J–V* characteristics correspondingly for the 'with HTL' and 'without HTL' structures of the optimized PSC. From Fig. 13(a), a noticeable decrease in QE occurred with the longer wavelength, whereas the insertion of a HTL remarkably enhanced the QE for shorter and longer wavelength photons. The photon absorption capacity increased from 82% to nearly 99.5% for the photon wavelength of 500 nm due to the insertion of the HTL. Also, the longer-wavelength photon absorption was enhanced by the insertion of the HTL. The insertion of the Sb_2S_3 HTL with an appropriate band gap and satisfactory band alignment next to the $RbGeI_3$ absorber layer dramatically advanced the absorption of light at longer wavelengths (>900 nm), which is the key reason why the cell performance increased from 19.42% to 30.35%.

The *J–V* curve is a well-organized tool for estimating the carrier's loss due to recombination in the SC. Fig. 13(b) shows that there was a dramatic increase in the V_{oc} and J_{sc} after simply inserting an appropriate HTL. The insertion of the HTL resulted in a lower value of current density by deducing the recombination of the minority carrier, and thereby enhancing V_{oc}, J_{sc}, and hence PCE. The maximum PCE of the optimized ('without HTL') PSC was 19.42%, which obeys the limitations of Shockley–Queisser (highest PCE 30% at 1.1 eV,[99] and highest PCE 33.16% at 1.34 eV[100]). Conversely, in this investigation, a boosted PCE of 30.35% was achieved by inserting an additional HTL.

On the basis of previous studies, the reason behind the improvement in cell performance for a double junction can be established by the TSA two-step photon upconversion process.[16,17,56] The sub-band gap photons are conspicuously engrossed in an arrangement by Urbach tail-states of materials that create further electron–hole pairs in the TSA process. As a

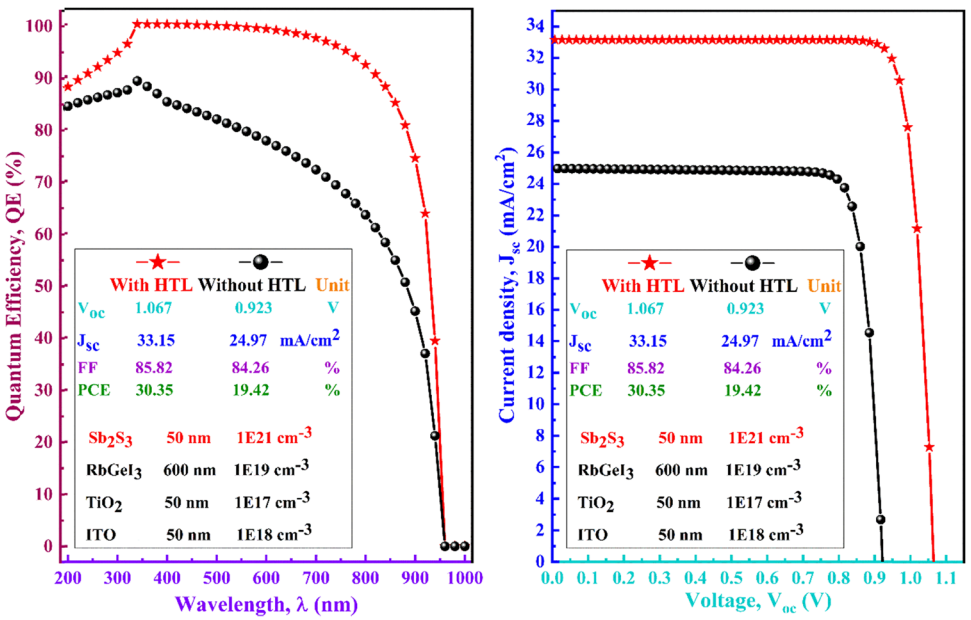

Fig. 13 (a) QE-wavelength curve and (b) *J–V* curve of the optimized $RbGeI_3$-based proposed PSC.

Table 8 Performance of the $RbGeI_3$-based PSC devices for different configurations

Sl. no. and ref.	Configuration	Types	V_{oc} (V)	J_{sc} (mA cm^{-2})	FF (%)	PCE (%)
01[26]	FTO/$RbGeI_3$/TiO_2/Ag	Theo.	0.291	25.386	48.637	3.601
02[101]	FTO/TiO_2/$RbGeI_3$/NiO/Ag	Theo.	0.5311	28.89	63.68	10.11
03[25]	ITO/$CuCrO_2$/$RbGeI_3$/TiO_2/Au	Theo.	0.89	33.70	79.20	23.80
04[102]	FTO/PCBM/$RbGeI_3$/PTAA/C	Theo.	0.8325	33.03193	79.8447	21.9567
05[a]	Al/ITO/TiO_2/$RbGeI_3$/Pt	Theo.	0.923	24.97	84.26	19.42
06[a]	Al/ITO/TiO_2/$RbGeI_3$/Sb_2S_3/Pt	Theo.	1.067	33.15	85.82	30.35

[a] Present investigation, Theo. = theoretical.

result, an HTL with a satisfactory band gap and carrier density and a higher coefficient of absorption might bring about an effective TSA upconversion process in the area of longer wavelengths,[16,17,56,79] which may be the key reason for the performance enhancement from 19.42% to 30.35%.

3.11.3 Optimized value of PV performance parameters. For the 'without HTL' structure, *i.e.*, Al/ITO/TiO_2/$RbGeI_3$/Pt, the optimized values of V_{oc}, J_{sc}, FF, and PCE were obtained as 0.923 V, 24.97 mA cm^{-2}, 84.26%, and 19.42%, respectively.

For the 'with HTL' structure, *i.e.*, Al/ITO/TiO_2/$RbGeI_3$/Sb_2S_3/Pt, the optimized values of V_{oc}, J_{sc}, FF, and PCE were obtained as 1.067 V, 33.15 mA cm^{-2}, 85.82%, and 30.35%, respectively, through numerical simulation with the SCAPS-1D simulator.

3.11.4 Comparison of the present investigation with prior work. The output performance of this investigation was compared with prior work. The output performance of different $RbGeI_3$-based PSC devices is listed in Table 8, which shows that the output performance of the proposed PSC device with its new structure has been comprehensively increased.

4. Conclusion

In this investigation, various HTMs and ETMs were incorporated into the Pb-free perovskite-based ($RbGeI_3$) absorber to discover the primary structure of the proposed SC device with higher performance. To evaluate the PV performance of the proposed PSC device for different structures, the SCAPS-1D simulator was utilized. After many trials, Al/ITO/TiO_2/$RbGeI_3$/Sb_2S_3/Pt proved to be an effective primary structure. After obtaining the finalized structure, different parameters such as temperature; work function of the left metal contact; series and shunt resistance; surface recombination velocity of holes and electrons; perovskite layer, ETM, and HTM thickness; perovskite layer, ETM, and HTM carrier concentration; defect density of the perovskite layer, ETM, and HTM; and HTL/absorber and absorber/ETL interface defect density were varied so that the proposed device would be more practical. For the 'without HTL' and 'with HTL' configurations, all the influencing factors were optimized. The optimized thickness of the ETL, absorber, and HTL for the 'without HTL' and 'with HTL' configurations was found to be 50 nm, 600 nm, and 50 nm, respectively. Also, the optimized carrier concentrations for the ETL, absorber, and HTL for 'without HTL' and 'with HTL' were found to be 10^{17} cm^{-3}, 10^{19} cm^{-3}, and 10^{21} cm^{-3}, respectively. Moreover, the temperature impact also ensured that the suggested device was unaffected by the typical operating temperature range of 300 K to 321 K. The optimized structure 'without HTL' showed optimal values for V_{oc}, J_{sc}, FF, and PCE of 0.923 V, 24.97 mA cm^{-2}, 84.26%, and 19.42%, respectively, whereas the optimized structure 'with HTL' showed optimal values for V_{oc}, J_{sc}, FF, and PCE of 1.067 V, 33.15 mA cm^{-2}, 85.82%, and 30.35%, respectively. Comparative performances with other structures were also studied, and the investigated new structure seems to be important in the long run for experimental designs.

Author contributions

Md. Mojahidur Rahman – conceived, designed, and performed the simulation process; analyzed and interpreted the data; prepared figures; and wrote the manuscript. Md. Hasan Ali – conceived, designed, analyzed, and interpreted the data; prepared figures; wrote, reviewed, and edited the manuscript. Md. Dulal Haque – conceived, designed, and analyzed the data; and reviewed the manuscript. Abu Zafor Md. Touhidul Islam – conceived, designed, and interpreted the data; and reviewed the manuscript.

List of abbreviations

Abbreviations	Elaborations
PV	Photovoltaic
TW	Terawatts
CTL	Charge transport layer
HTL	Hole transport layer
ETL	Electron transport layer
FF	Fill factor
PCE	Power conversion efficiency
QE	Quantum efficiency
PGC	Photo generated carrier
PGH	Photo generated hole
PGE	Photo generated electron
PSC	Perovskite solar cell
CB	Conduction band
VB	Valence band
CTM	Charge transport material
HTM	Hole transport material
ETM	Electron transport material
TSA	Tail-states-assisted

List of symbols

Symbols	Meaning
L	Thickness
E_g	Band gap
χ	Electron affinity
ε_r	Dielectric permittivity (relative)
N_C	CB effective density of states
N_V	VB effective density of states
$\nu_{T,n}$	Electron thermal velocity
$\nu_{T,p}$	Hole thermal velocity
μ_n	Electron mobility
μ_p	Hole mobility
N_D	Shallow uniform donor density
N_A	Shallow uniform acceptor density
σ_n	Capture cross section (electrons)
σ_p	Capture cross section (holes)
N_t	Total defect density (bulk)
n_t	Total defect density (interface)
R_s	Series resistance
R_{sh}	Shunt resistance
Φ	Work function

ε_0	Dielectric permittivity (vacuum)
ρ_p	Hole distribution
ρ_n	Electron distribution
J_p	Hole current density
J_n	Electron current density
J_{sc}	Short circuit current density
J_o	Reverse bias saturation current density
q	Charge of an electron
n	Diode ideality factor
k	Boltzmann constant
T	Ambient temperature
V_{oc}	Open circuit voltage
η	Power conversion efficiency

Data availability

The data that has been used is confidential. The data will be available upon reasonable request to the corresponding author(s).

Conflicts of interest

There are no conflicts of interest among the authors.

Acknowledgements

This research has not been funded by any research organization or university. The authors express their heartfelt appreciation to Dr Marc Burgelman and his colleagues at the EIS Department at the University of Gent in Belgium for providing us with the opportunity to conduct research using the SCAPS-1D software.

References

1 M. H. Ali, M. A. Al Mamun, M. D. Haque, M. F. Rahman, M. K. Hossain and A. Z. Abu, Performance Enhancement of an MoS_2-Based Heterojunction Solar Cell with an In_2Te_3 Back Surface Field: A Numerical Simulation Approach, *ACS Omega*, 2023, **8**(7), 7017–7029.

2 H. Chen, Z. Wang, S. Xu, Y. Zhao, Q. Cheng and B. Zhang, Energy demand, emission reduction and health co-benefits evaluated in transitional China in a 2 °C warming world, *J. Cleaner Prod.*, 2020, **264**, 121773.

3 Y. Yu, N. Zhang and J. D. Kim, Impact of urbanization on energy demand: an empirical study of the Yangtze River Economic Belt in China, *Energy Policy*, 2020, **139**, 111354.

4 C. A. Wolden, J. Kurtin, J. B. Baxter, I. Repins, S. E. Shaheen, J. T. Torvik, A. A. Rockett, V. M. Fthenakis and E. S. Aydil, Photovoltaic manufacturing: present status, future prospects, and research needs, *J. Vac. Sci. Technol., A*, 2011, **29**(3), 030801.

5 D. Meissner, Solar Power Implications of our Climate Crisis, Source: **https://www.quantsol.org/pub/pub11_08.pdf**.

6 S. Ahmmed, A. Aktar, M. H. Rahman, J. Hossain and A. B. Abu, Design and simulation of a high-performance $CH_3NH_3Pb(I_{1-x}Cl_x)_3$-based perovskite solar cell using a CeO_x electron transport layer and NiO hole transport layer, *Semicond. Sci. Technol.*, 2021, **36**(3), 035002.

7 M. Spalla, L. Perrin, E. Planes, M. Matheron, S. Berson and L. Flandin, Effect of the Hole Transporting/Active Layer Interface on the Perovskite Solar Cell Stability', *ACS Appl. Energy Mater.*, 2020, **3**(4), 3282–3292.

8 J. Y. Kim, J.-W. Lee, H. S. Jung, H. Shin and N. G. Park, High-Efficiency Perovskite Solar Cells, *Chem. Rev.*, 2020, **120**(15), 7867–7918.

9 A. Kuddus, M. F. Rahman, J. Hossain and A. B. M. Ismail, Enhancement of the performance of CdS/CdTe heterojunction solar cell using TiO_2/ZnO bi-layer ARC and V_2O_5 BSF layers: a simulation approach, *EPJ Appl. Phys.*, 2020, **92**(2), 20901.

10 M. A. Rahman, Design and simulation of a high-performance Cd-free Cu_2SnSe_3 solar cells with SnS electron-blocking hole transport layer and TiO_2 electron transport layer by SCAPS-1D, SN, *Appl. Sci.*, 2021, **3**(2), 253.

11 M. M. Lee, J. Teuscher, T. Miyasaka, T. N. Murakami and H. J. Snaith, Efficient Hybrid Solar Cells Based on Meso-Superstructured Organometal Halide Perovskites, *Science*, 1979, **2012338**(6107), 643–647.

12 B. Conings, J. Drijkoningen, N. Gauquelin, A. Babayigit, J. D'Haen, L. D'Olieslaeger, A. Ethirajan, J. Verbeeck, J. Manca, E. Mosconi and F. D. Angelis, Intrinsic Thermal Instability of Methylammonium Lead Trihalide Perovskite, *Adv. Energy Mater.*, 2015, **5**(15), 1500477.

13 I. Hanif, S. M. Faraz Raza, P. Gago-de-Santos and Q. Abbas, Fossil fuels, foreign direct investment, and economic growth have triggered CO_2 emissions in emerging Asian economies: some empirical evidence, *Energy*, 2019, **171**, 493–501.

14 A. Kuddus, S. K. Mostaque and J. Hossain, Simulating the performance of a high-efficiency SnS-based dual-heterojunction thin film solar cell, *Opt. Mater. Express*, 2012, **11**(11), 3812.

15 S. K. Mostaque, B. K. Mondal and J. Hossain, Numerical simulation on the impurity photovoltaic (IPV) effect in c-Si wafer-based dual-heterojunction solar cell, *Mater. Today Commun.*, 2022, **33**, 104442.

16 A. Kuddus, A. B. M. Ismail and J. Hossain, Design of a highly efficient CdTe-based dual-heterojunction solar cell with 44% predicted efficiency, *Sol. Energy*, 2021, **221**, 488–501.

17 B. K. Mondal, S. K. Mostaque and J. Hossain, Theoretical insights into a high-efficiency Sb_2 Se_3-based dual-heterojunction solar cell, *Heliyon*, 2022, **8**(3), E09120.

18 M. Mostefaoui, H. Mazari, S. Khelifi, A. Bouraiou and R. Dabou, Simulation of High Efficiency CIGS Solar Cells with SCAPS-1D Software, *Energy Procedia*, 2015, **74**, 736–744.

19 S. K. Mostaque, B. K. Mondal and J. Hossain, Simulation approach to reach the SQ limit in CIGS-based dual-heterojunction solar cell, *Optik*, 2022, **249**, 168278.

20 M. S. Rana, M. M. Islam and M. Julkarnain, Enhancement in efficiency of CZTS solar cell by using CZTSe BSF layer, *Sol. Energy*, 2021, **226**, 272–287.
21 Y. H. Khattak, F. Baig, S. Ullah, B. Marí, S. Beg and H. Ullah, Numerical modeling baseline for high efficiency (Cu_2FeSnS_4) CFTS based thin film kesterite solar cell, *Optik*, 2018, **164**, 547–555.
22 F. Kouadio Konan, H. Joël Tchognia Nkuissi and B. Hartiti, Numerical Simulations of Highly Efficient Cu_2FeSnS_4 (CFTS) Based Solar Cells, *Int. J. Renewable Energy Res.*, 2019, **9**(4), 1865–1872.
23 M. D. A. H. Pappu, A. Kuddus, B. K. Mondal, A. T. Abir and J. Hossain, Design of n-CdS/p-$CuInTe_2$/p^+-MoS_2 thin film solar cell with a power conversion efficiency of 34.32%, *Opt. Continuum*, 2023, **2**(4), 942.
24 D. K. Sarkar, M. Mottakin, A. K. Mahmud Hasan, V. Selvanathan, K. Sobayel, M. N. I. Khan, A. F. M. Masum Rabbani, M. Shahinuzzaman, M. Aminuzzaman, F. H. Anuar, T. Suemasu, K. Sopian and Md Akhtaruzzaman, A comprehensive study on $RbGeI_3$ based inorganic perovskite solar cell using green synthesized $CuCrO_2$ as hole conductor, *J. Photochem. Photobiol., A*, 2023, **439**, 114623.
25 G. Pindolia, S. M. Shinde and P. K. Jha, Optimization of an inorganic lead free $RbGeI_3$ based perovskite solar cell by SCAPS-1D simulation, *Sol. Energy*, 2022, **236**, 802–821.
26 M. T. Ekwu, E. Danladi, N. N. Tasie, I. S. Haruna, O. E. Okoro, P. M. Gyuk, O. M. Jimoh and R. C. Obasi, A QUALITATIVE THEORETICAL STUDY OF INORGANIC HTM-FREE $RbGeI_3$ BASED PEROVSKITE SOLAR CELLS USING SCAPS-1D AS A PATHWAY TOWARDS 3.601% EFFICIENCY, East, *Eur. J. Phys.*, 2023, **2023**(1), 118–124.
27 A. Kojima, K. Teshima, Y. Shirai and T. Miyasaka, Organometal halide perovskites as visible-light sensitizers for photovoltaic cells, *J. Am. Chem. Soc.*, 2009, **131**(17), 6050–6051.
28 W. Ke and M. G. Kanatzidis, Prospects for low-toxicity lead-free perovskite solar cells, *Nat. Commun.*, 2019, **10**(1), 965.
29 N. K. Noel, N. K. Noel, S. D. Stranks, A. Abate, C. Wehrenfennig, S. Guarnera, A. A. Haghighirad, A. Sadhanala, G. E. Eperon, S. K. Pathak, M. B. Johnston and A. Petrozza, Lead-free organic–inorganic tin halide perovskites for photovoltaic applications, *Energy Environ. Sci.*, 2014, **7**(9), 3061–3068.
30 G. Thiele, H. W. Rotter and K. D. Schmidt, Die Kristallstrukturen und Phasentransformationen des tetramorphen $RbGeI_3$, *Zeitschrift für anorganische und all gemeine Chemie*, 1989, **571**(1), 60–68.
31 B. M. Wong and J. G. Cordaro, Coumarin dyes for dye-sensitized solar cells: a long-range-corrected density functional study, *J. Chem. Phys.*, 2008, **129**(21), 214703.
32 K. A. Parrey, T. Farooq, S. A. Khandy, U. Farooq and A. Gupta, First principle studies on structure, magneto-electronic and elastic properties of photovoltaic semiconductor halide ($RbGeI_3$) and ferromagnetic half metal oxide ($RbDyO_3$), *Comput. Condens. Matter*, 2019, **19**, E00381.
33 U.-G. Jong, C.-J. Yu, Y.-H. Kye, Y.-G. Choe, W. Hao and S. Li, First-Principles Study on Structural, Electronic, and Optical Properties of Inorganic Ge-Based Halide Perovskites, *Inorg. Chem.*, 2019, **58**(7), 4134–4140.
34 K. Deepthi Jayan and V. Sebastian, Ab initio DFT determination of structural, mechanical, optoelectronic, thermoelectric and thermodynamic properties of $RbGeI_3$ inorganic perovskite for different exchange-correlation functionals, *Mater. Today Commun.*, 2021, **28**, 102650.
35 Z. Qin, Y. Zhang and J. Guo, SCAPS simulation and DFT study of ultra-thin lead-free perovskite solar cells based on $RbGeI_3$, *Opt. Commun.*, 2024, **554**, 130187.
36 A. Kowsar, M. Billah, S. Dey, S. C. Debnath, S. Yeakin and S. F. Uddin Farhad, Comparative Study on Solar Cell Simulators, *2019 2nd International Conference on Innovation in Engineering and Technology (ICIET)*, IEEE, 2019, pp. 1–6.
37 A. Kowsar, S. N. Sakib, M. B. Billah, S. Dey, K. N. Babi, A. N. Bahar and S. F. Farhad, A novel simulator of multi-junction solar cells MSCS-1D, *Int. J. Renewable Energy Res.*, 2020, **10**(3), 1369–1375.
38 M. A. Rahman, Numerical modeling of ultra-thin $CuSbS_2$ heterojunction solar cell with TiO_2 electron transport and $CuAlO_2$:Mg BSF layers, *Opt. Mater. Express*, 2022, **12**(8), 2954.
39 A. Isha, *et al.*, High efficiency Cu_2MnSnS_4 thin film solar cells with SnS BSF and CdS ETL layers: a numerical simulation, *Heliyon*, 2023, **9**(5), E15716.
40 U. C. Obi, *Investigation Of Lead-Free Bismuth Perovskite By Numerical*, African University Of Science And Technology, Abuja, PhD. diss., 2019.
41 B. M. Soucase, I. Guaita Pradas and K. R. Adhikari, Numerical Simulations on Perovskite Photovoltaic Devices, *Perovskite Materials: Synthesis, Characterisation, Properties, and Applications*, 2016, ch. 15, pp. 445–488.
42 M. Minbashi, A. Ghobadi, M. H. Ehsani, H. Rezagholipour Dizaji and N. Memarian, Simulation of high efficiency SnS-based solar cells with SCAPS, *Sol. Energy*, 2018, **176**, 520–525.
43 M. Burgelman, J. Verschraegen, S. Degrave and P. Nollet, Modeling thin-film PV devices, *Prog. Photovoltaics Res. Appl.*, 2004, **12**(23), 143–153.
44 M. Burgelman, J. Verschraegen, B. Minnaert and J. Marlein, Numerical simulation of thin film solar cells: practical exercises with SCAPS, *Proceedings of NUMOS (Int. Workshop on Numerical Modeling of Thin Film Solar Cells, Gent (B)), Gent.*, U Gent & Academia Press, 2007.
45 Y. Kawano, J. Chantana and T. Minemoto, Impact of growth temperature on the properties of SnS film prepared by thermal evaporation and its photovoltaic performance, *Curr. Appl. Phys.*, 2015, **15**(8), 897–901.
46 H. Movla, Optimization of the CIGS based thin film solar cells: numerical simulation and analysis, *Optik*, 2014, **125**(1), 67–70.
47 A. Niemegeers, S. Gillis and M. Burgelman, A user program for realistic simulation of polycrystalline heterojunction solar cells: SCAPS-1D, Proceedings of the 2nd World Conference on Photovoltaic Energy Conversion, JRC, European Commission, juli, 1998, 672–675.

48 M. Yoshitake, *Work Function and Band Alignment of Electrode Materials*, National Institute for Materials Science, Japan, 2021.
49 J. Hsizl and F. K. Schulte, Work Function of Metals, *Springer Tracts in Modern Physics*, 2006, vol. 85, pp. 1–150.
50 K. Ali and Z. Ali, Analytical study of electrical performance of SiGe-based n^+–p–p^+ solar cells with $BaSi_2$ BSF structure, *Sol. Energy*, 2021, **225**, 91–96.
51 C. Doroody, *et al.*, Impact of Back Surface Field (BSF) Layers in Cadmium Telluride (CdTe) Solar Cells from Numerical Calculation, *Int. J. Recent Technol. Eng.*, 2019, **8**(4), 6218–6222.
52 Md. N. H. Riyad, A. Sunny, M. M. Khatun, S. Rahman and S. R. Al Ahmed, Performance evaluation of WS_2 as buffer and Sb_2S_3 as hole transport layer in CZTS solar cell by numerical simulation, *Eng. Rep.*, 2023, **5**(5), E12600.
53 M. K. Hossain, M. H. K. Rubel, G. F. I. Toki, I. Alam, M. F. Rahman and H. Bencherif, Effect of Various Electron and Hole Transport Layers on the Performance of $CsPbI_3$-Based Perovskite Solar Cells: A Numerical Investigation in DFT, SCAPS-1D, and wxAMPS Frameworks, *ACS Omega*, 2022, **7**(47), 43210–43230.
54 S. Yasin, Z. A. Waar, T. Al Zoubi and M. Moustafa, Optoelectronic simulation of a high efficiency C_2N based solar cell via buffer layer optimization, *Opt. Mater.*, 2021, **119**, 111364.
55 S. Tripathi, Sadanand, P. Lohia and D. K. Dwivedi, Contribution to sustainable and environmental friendly non-toxic CZTS solar cell with an innovative hybrid buffer layer, *Sol. Energy*, 2020, **204**, 748–760.
56 B. K. Mondal, S. K. Mostaque, M. A. Rashid, A. Kuddus, H. Shirai and J. Hossain, Effect of CdS and In_3Se_4 BSF layers on the photovoltaic performance of PEDOT:PSS/n-Si solar cells: simulation based on experimental data, *Superlattices Microstruct.*, 2021, **152**, 106853.
57 F. Belarbi, W. Rahal, D. Rached, S. Benghabrit and M. Adnane, A comparative study of different buffer layers for CZTS solar cell using Scaps-1D simulation program, *Optik*, 2020, **216**, 164743.
58 K. Kanchan, A. Sahu and B. Kumar, Numerical Simulation of Copper Indium Gallium Diselenide Solar Cell with Ultra-Thin $BaSi_2$ Back Surface Field Layer Using the Non-Toxic In_2Se_3 Buffer Layer, *Silicon*, 2022, **14**(18), 12675–12682.
59 H. A. Mohamed, Dependence of efficiency of thin-film CdS/CdTe solar cell on optical and recombination losses, *J. Appl. Phys.*, 2013, **113**(9), 093105.
60 N. R. Paudel, K. A. Wieland and A. D. Compaan, Ultrathin CdS/CdTe solar cells by sputtering, *Sol. Energy Mater. Sol. Cells*, 2012, **105**, 109–112.
61 P. Singh and N. M. Ravindra, Temperature dependence of solar cell performance—an analysis, *Sol. Energy Mater. Sol. Cells*, 2012, **101**, 36–45.
62 Z. Hawash, L. K. Ono, S. R. Raga, M. V. Lee and Y. Qi, Air-Exposure Induced Dopant Redistribution and Energy Level Shifts in Spin-Coated Spiro-MeOTAD Films, *Chem. Mater.*, 2015, **27**(2), 562–569.
63 A. F. Akbulatov, *et al.*, Effect of Electron-Transport Material on Light-Induced Degradation of Inverted Planar Junction Perovskite Solar Cells, *Adv. Energy Mater.*, 2017, **7**(19), 1700476.
64 A. K. Jena, Y. Numata, M. Ikegami and T. Miyasaka, Role of spiro-OMeTAD in performance deterioration of perovskite solar cells at high temperature and reuse of the perovskite films to avoid Pb-waste, *J. Mater. Chem. A*, 2018, **6**(5), 2219–2230.
65 K. Norrman, M. V. Madsen, S. A. Gevorgyan and F. C. Krebs, Degradation Patterns in Water and Oxygen of an Inverted Polymer Solar Cell, *J. Am. Chem. Soc.*, 2010, **132**(47), 16883–16892.
66 J. Liang, *et al.*, All-Inorganic Perovskite Solar Cells, *J. Am. Chem. Soc.*, 2016, **138**(49), 15829–15832.
67 N. A. N. Ouedraogo, Stability of all-inorganic perovskite solar cells, *Nano Energy*, 2020, **67**, 104249.
68 A. K. Singh, S. Srivastava, A. Mahapatra, J. K. Baral and B. Pradhan, Performance optimization of lead free-$MASnI_3$ based solar cell with 27% efficiency by numerical simulation, *Opt. Mater.*, 2021, **117**, 111193.
69 H. Wei, *et al.*, Challenges and strategies of all-inorganic lead-free halide perovskite solar cells, *Ceram. Int.*, 2022, **48**(5), 5876–5891.
70 A. Tara, V. Bharti, S. Sharma and R. Gupta, Device simulation of $FASnI_3$ based perovskite solar cell with $Zn(O_{0.3},S_{0.7})$ as electron transport layer using SCAPS-1D, *Opt. Mater.*, 2021, **119**, 111362.
71 A. Ghosh, S. S. Dipta, S. S. S. Nikor, N. Saqib and A. Saha, Performance analysis of an efficient and stable perovskite solar cell and a comparative study of incorporating metal oxide transport layers, *J. Opt. Soc. Am. B*, 2020, **37**(7), 1966.
72 D. Saikia, J. Bera, A. Betal and S. Sahu, Performance evaluation of an all inorganic $CsGeI_3$ based perovskite solar cell by numerical simulation, *Opt. Mater.*, 2022, **123**, 111839.
73 J. Barbé, *et al.*, Amorphous Tin Oxide as a Low-Temperature-Processed Electron-Transport Layer for Organic and Hybrid Perovskite Solar Cells, *ACS Appl. Mater. Interfaces*, 2017, **9**(13), 11828–11836.
74 K. K. Subedi, *et al.*, Enabling bifacial thin film devices by developing a back surface field using Cu_xAlO_y, *Nano Energy*, 2021, **83**, 105827.
75 L. Lin, L. Jiang, P. Li, B. Fan and Y. Qiu, A modeled perovskite solar cell structure with a Cu_2O hole-transporting layer enabling over 20% efficiency by low-cost low-temperature processing, *J. Phys. Chem. Solids*, 2019, **124**, 205–211.
76 M. K. Hossain, S. Bhattarai, A. A. Arnab, M. K. Mohammed, R. Pandey, M. H. Ali, M. F. Rahman, M. R. Islam, D. P. Samajdar, J. Madan and H. Bencherif, Harnessing the potential of $CsPbBr_3$-based perovskite solar cells using efficient charge transport materials and global optimization, *RSC Adv.*, 2023, **13**(30), 21044–21062.
77 A. Chatterjee, S. Biswas and A. Sinha, Tunneling Current of an AlGaAs/GaAs Multiple-Quantum-well Solar Cell

Considering a Trapezoidal Potential Barrier, *Int. J. Renewable Energy Res.*, 2018, **8**(2), 672–681.

78 J. Hossain, M. M. A. Moon, B. K. Mondal and M. A. Halim, Design guidelines for a highly efficient high-purity germanium (HPGe)-based double-heterojunction solar cell, *Opt Laser Technol.*, 2021, **143**, 107306.

79 J. Hossain, B. K. Mondal and S. K. Mostaque, Computational investigation on the photovoltaic performance of an efficient GeSe-based dual-heterojunction thin film solar cell, *Semicond. Sci. Technol.*, 2022, **37**(1), 015008.

80 S. Ahmmed, A. Aktar, J. Hossain and A. B. M. Ismail, Enhancing the open circuit voltage of the SnS based heterojunction solar cell using NiO HTL, *Sol. Energy*, 2020, **207**, 693–702.

81 M. M. Khatun, A. Sunny and S. R. Al, Ahmed, Numerical investigation on performance improvement of WS_2 thin-film solar cell with copper iodide as hole transport layer, *Sol. Energy*, 2021, **224**, 956–965.

82 S. Kohnehpoushi, P. Nazari, B. A. Nejand and M. Eskandari, MoS_2: a two-dimensional hole-transporting material for high-efficiency, low-cost perovskite solar cells, *Nanotechnology*, 2018, **29**(20), 205201.

83 S. Taheri, A. Ahmadkhan kordbacheh, M. Minbashi and A. Hajjiah, Effect of defects on high efficient perovskite solar cells, *Opt. Mater.*, 2021, **111**, 110601.

84 M. S. S. Basyoni, *et al.*, On the Investigation of Interface Defects of Solar Cells: Lead-Based vs Lead-Free Perovskite, *IEEE Access*, 2021, **9**, 130221–130232.

85 N. Jensen, R. M. Hausner, R. B. Bergmann, J. H. Werner and U. Rau, Optimization and characterization of amorphous/crystalline silicon heterojunction solar cells, *Prog. Photovoltaics Res. Appl.*, 2002, **10**(1), 1–13.

86 M. K. Hossain, *et al.*, Numerical Analysis in DFT and SCAPS-1D on the Influence of Different Charge Transport Layers of $CsPbBr_3$ Perovskite Solar Cells, *Energy Fuels*, 2023, **37**(8), 6078–6098.

87 Y. Li, *et al.*, Ultra-high open-circuit voltage of perovskite solar cells induced by nucleation thermodynamics on rough substrates, *Sci. Rep.*, 2017, **7**(1), 46141.

88 Y. Galagan, E. W. C. Coenen, W. J. H. Verhees and R. Andriessen, Towards the scaling up of perovskite solar cells and modules, *J. Mater. Chem. A*, 2016, **4**(15), 5700–5705.

89 S. M. Sze, Y. Li and K. K. Ng, *Physics of semiconductor devices*, John Wiley & Sons, 2021.

90 I. Mora-Seró, G. Garcia-Belmonte, P. P. Boix, M. A. Vázquez and J. Bisquert, Impedance spectroscopy characterisation of highly efficient silicon solar cells under different light illumination intensities, *Energy Environ. Sci.*, 2009, **2**(6), 678–686.

91 G. G. Malliaras, J. R. Salem, P. J. Brock and C. Scott, Electrical characteristics and efficiency of single-layer organic light-emitting diodes, *Phys. Rev. B: Condens. Matter Mater. Phys.*, 1998, **58**(20), R13411.

92 G. K. Gupta, A. Garg and A. Dixit, Electrical and impedance spectroscopy analysis of sol-gel derived spin coated Cu_2ZnSnS_4 solar cell, *J. Appl. Phys.*, 2018, **123**(1), 013101.

93 R. K. Zahoo, Effect of carrier concentration and thickness of absorber layer on performance CBTS solar cell, *Turkish J. Comput. Math. Educ.*, 2021, **12**(10), 5056–5064.

94 H. B. Michaelson, The work function of the elements and its periodicity, *J. Appl. Phys.*, 1977, **48**(11), 4729–4733.

95 S. R. Al Ahmed, A. Sunny and S. Rahman, Performance enhancement of Sb_2Se_3 solar cell using a back surface field layer: a numerical simulation approach, *Sol. Energy Mater. Sol. Cells*, 2021, **221**, 110919.

96 N. Singh, A. Agarwal and M. Agarwal, Numerical simulation of highly efficient lead-free perovskite layers for the application of all-perovskite multi-junction solar cell, *Superlattices Microstruct.*, 2021, **149**, 106750.

97 S. Ahmmed, *et al.*, Performance analysis of lead-free $CsBi_3I_{10}$-based perovskite solar cell through the numerical calculation, *Sol. Energy*, 2021, **226**, 54–63.

98 S. Ahmed, F. Jannat, Md. A. K. Khan and M. A. Alim, Numerical development of eco-friendly Cs_2TiBr_6 based perovskite solar cell with all-inorganic charge transport materials via SCAPS-1D, *Optik*, 2021, **225**, 165765.

99 W. Shockley and H. J. Queisser, Detailed Balance Limit of Efficiency of p–n Junction Solar Cells, *J. Appl. Phys.*, 1961, **32**(3), 510–519.

100 S. Rühle, Tabulated values of the Shockley–Queisser limit for single junction solar cells, *Sol. Energy*, 2016, **130**, 139–147.

101 D. K. Sarkar, *et al.*, A comprehensive study on $RbGeI_3$ based inorganic perovskite solar cell using green synthesized $CuCrO_2$ as hole conductor, *J. Photochem. Photobiol., A*, 2023, **439**, 114623.

102 G. Pindolia, S. M. Shinde and P. K. Jha, Void of lead and non-carcinogenic germanium based $RbGeI_3$ PSC using organic charge transport layers: towards a clean and green future, *J. Mater. Sci.: Mater. Electron.*, 2023, **34**(9), 804.